UCLA

UCLA Electronic Theses and Dissertations

Title
Super resolution of Optical Fluctuation Imaging 2.0 (SOFI-2.0): Towards fast super resolved imaging of live cells

Permalink
https://escholarship.org/uc/item/5xs5v4qm

Author
Yi, Xiyu

Publication Date
2017

Supplemental Material
https://escholarship.org/uc/item/5xs5v4qm#supplemental

Peer reviewed|Thesis/dissertation

UNIVERSITY OF CALIFORNIA

Los Angeles

Super resolution of Optical Fluctuation Imaging 2.0 (SOFI-2.0):

Towards fast super resolved imaging of live cells

A dissertation submitted in partial satisfaction of the

requirements for the degree Doctor of Philosophy

in Chemistry

by

Xiyu Yi

2017

ABSTRACT OF THE DISSERTATION

Super resolution of Optical Fluctuation Imaging 2.0 (SOFI-2.0):

Towards fast super resolved imaging of live cells

by

Xiyu Yi

Doctor of Philosophy in Chemistry

University of California, Los Angeles, 2017

Professor Shimon Weiss, Chair

Super resolution Optical Fluctuation Imaging (SOFI) has been widely acknowledged and advanced over the past years. Comparing to other extensively adopted super resolution techniques such as PALM, STORM, STED and SIM, advantages of SOFI include compatibility with different imaging platforms, suitability for a wide variety of probes, flexibility in imaging conditions, and a user-controlled trade-off between spatial- and temporal- resolutions. SOFI therefore holds great promise for 'democratizing' super resolution imaging for broad applications by non-expert practitioners. The theoretical resolution enhancement of SOFI scales as the square root of the cumulant order n, and once combined with a post-processing deconvolution algorithm, the resolution enhancement factor increases up to n. In this dissertation I will discuss the fundamental challenges faced by high order SOFI applications including pixel intensity dynamic range expansion, associated artifacts, point-spread function (PSF) estimation, and deconvolution. Several approaches for solving these challenges will be

presented, that together constitute what we dub as 'SOFI-2.0'. The power of SOFI-2.0 will be demonstrated for focal-adhesion dynamics (at super resolution) in live cells.

The dissertation of Xiyu Yi is approved.

Xiangfeng Duan

William M. Gelbart

Luminita Vese

Shimon Weiss, Committee Chair

University of California, Los Angeles

2017

DEDICATION

I would like to dedicate this work to my family, friends and fellow students, as well as group

members who were always supportive and encouraging and help to made this work possible.

Table of Contents

ACKNOWLEDGEMENT

VITA /BIOGRAPHICAL SKETCH

EDUCATION

- 2012/01 – 2017/03 (Ph. D as expected)

  University of California, Los Angeles. Department of Chemistry and Biochemistry

- 2007/01 – 2011/06 (Bachelor's degree)

  Sichuan University of China, Department of Materials Science and Engineering

RESEARCH EXPERIENCE

- 2012/12 – 2017/03   Super-resolution Optical Fluctuation Imaging (SOFI)

  Mentor: Prof. Shimon Weiss

  Department of Chemistry and Biochemistry, UCLA, USA

- 2008/09 – 2011/07   Monte-Carlo simulation of the growth of single copper crystals.

  Mentor: Prof. Beijung Zhao

  Department of Material Science and Engineering, SCU, CHINA

PUBLICATIONS

- Kisley, L., Brunetti, R., Tauzin, L.J.., Shuang, B., Yi, X., Kirkeminde, A.W., Higgins, D.A., Weiss, S. and Landes, C.F., 2015. Characterization of porouse materials by fluorescence correlation spectroscopy super-resolution optical fluctuation imaging. ACS nano, 9(9), pp.9158-9166

- Solomon, O., Mutzafi, M., Yi, X., Weiss, S., Eldar, Y.C. and Segev, M., 2016, June. Sparsity-based super-resolution optical fluctuation imaging. In CLEO: Applications and Technology (pp. AM4O-4). Optical Society of America.

- Schidorsky, S., Yi, X., Razvag, Y., Golan, Y., Weiss, S. and Sherman, E., 2016. Synergizing superresolution optical fluctuation imaging with single molecule localization microscopy. ArXiv preprint arXiv:1603.0402

Chapter 1. Introduction of optical super resolution

Fluorescence microscopy is one of the most extensively used technologies in biology studies due to its capability to visualize specific biological structure at cellular and sub-cellular level. However, the spatial resolution of fluorescence microscopy is limited due to the diffraction limit of light, described as the Abbe's diffraction limit [1.1] described as follows:

$$d = \frac{\lambda}{2\,NA} \tag{1.1}$$

Where λ is the emission wavelength and NA is the numerical aperture of the optical system. Over the past decades, multiple techniques have been developed to break the diffraction limit of light to achieve super-resolution in fluorescence microscopy. Pioneering methods include Photo-activated Localization Microscopy (PALM)[1.2], Stochastic Optical Reconstruction Microscopy (STORM)[1.3], Stimulated Emission and Depletion Microscopy (STED)[1.4], Structure Illumination Microscopy (SIM)[1.5-1.7]. The principals of PALM and STORM in terms of reconstruction algorithms are similar, and belong to the family of Single Molecule Localization Microscopy (SMLM). Over the past decade many advanced versions of the methods have been developed to further push the super-resolution technology to further increase both the spatial and time resolution, as well as extending the super-resolution technology to three dimensions. In this chapter, an introductory discussion of the widely acknowledged super-resolution technologies will be discussed.

1.1.   Single Molecule Localization Microscopy (SMLM)

Single molecule localization microscopy achieves super-resolution through localization fitting of individual emitters. Two of the most widely acknowledged method within this family is PALM and STORM. In the practice of single molecule localization as illustrated in Figure 1.1, the feature of interest is labeled with fluorescence fluorophore, common fluorophores include quantum dots, fluorescence proteins and organic dyes. These fluorophores are then chemically or optically manipulated such that at given time instance, only a small portion of the fluorophores will be bright and form an image with a sparse distribution of individual fluorophores. Different images are captured at different time instances as consecutive frames to form a movie. For each frame in the acquired movie, single fluorophores are identified, and single molecule localization fitting is performed to find the locations of the fluorophores. After finding all the location of the fluorophores, these locations are super-imposed together to form the output image with super-resolution.
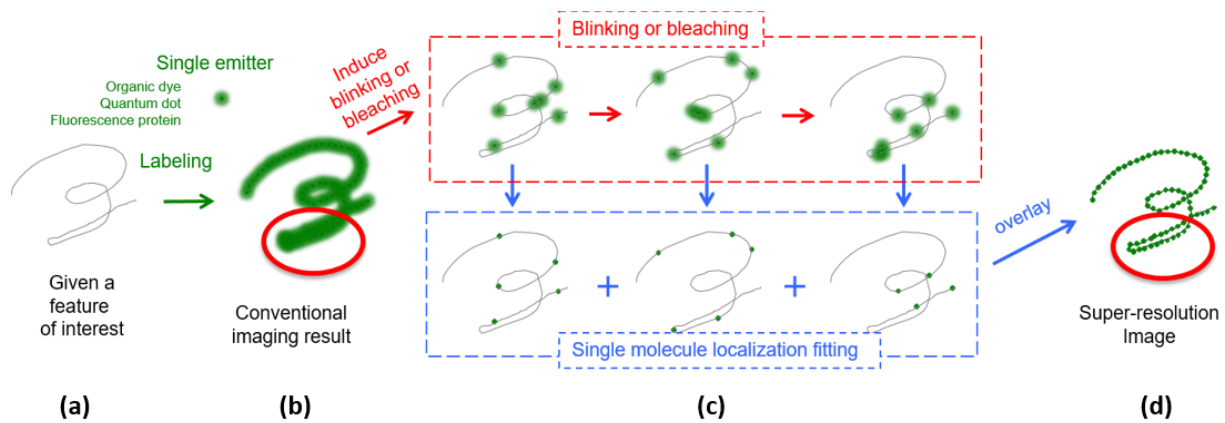
Figure 1.1. Concept of Single Molecule Localization Microscopy (SMLM).

Given a feature of interest as shown in (a), fluorescence labeling was performed. Due to the diffraction limit of light, the image of each individual fluorophore will be a diffraction limited point spread function, thus the conventional imaging result is diffraction limited as shown in (b). Blinking or bleaching is then induced in the fluorophores to achieve a small portion of bright fluorophores at a time instance. Different portion of emitters will be bright at different time instances, and captured in different frames in the acquired movie as shown in the upper panel of (c). Each single molecule is then identified and fitted to find the location of the fluorophores as shown in the lower panel in (c). All the localization results are super-imposed together to form the final super-resolution imaging as shown in (d). The single molecule localization microscopy provides super-resolution capability to resolve feature of interest that is too small to be observed with conventional imaging technique, as illustrated in the area with red circle in panel (b) and (c).

1.2. PALM and STORM

Two of the most extensively adopted single molecule localization microscopy method is Photo-activated Localization Microscopy (PALM) and Stochastic Optical Reconstruction Microscopy (STORM). The major difference between these two method is the way to achieve a sparse population of bright fluorophores in in a single frame of the acquired movie, and will be discussed separately as follows:

Photo-activated Localization Microscopy (PALM)

PALM was initially introduced by Betzig, E. et al. in 2006 [1.2] that takes advantage of the bleaching and activation properties of photoactivable fluorescence proteins (FA-FPs). In the practice of PALM, FA-FPs are used to label the feature of interest. Two lasers are used to achieve an optical density of bright emitters at given time instance, where one laser is responsible for the excitation and bleaching of the FA-PAs and we call it the excitation/bleaching laser, the other laser is responsible for activation of the FA-PAs, we call it activation laser. The special property of FA-FPs here is that the fluorescence protein generally has two different state, one is active and the other one is inactive state as illustrated in Figure 1.2. When the fluorescence protein is in its active state, it can absorb the photons supplied by the excitation laser, and being excited to emit light. In addition, this excitation laser can also turn the activated fluorescence protein into bleached state such that it will no longer be able to emit light. When the fluorescence protein is at its inactive state, it will not response to the excitation laser thus remains dark at the presence of excitation laser, however it can be activated by the activation laser and be turned into active state. The activation process is random and the rate is dependent on the activation laser power. As illustrated in Figure 1.3, at the initial imaging stage, in the FA-FP labeled sample, it is considered that only a

small portion of the fluorescence proteins are in the active states that can respond to the excitation/bleaching laser. The excitation/bleaching laser is initially turned on and maintained, only the activate FA-FPs will emit light and form images with sparse single molecules in the field of view. Consecutive frames are recorded, from which single molecule localization will be performed to each identified single molecules in each frame. As the excitation/bleaching laser is maintained, more and more FA-FPs are turned into the bleached state thus the total concentration of single molecules will decrease until the density is considered to be larger than the density requirement for single molecule identification. Then the activation laser is supplied in the form of a pulse. During this pulse, a small portion of the previously inactive fluorescence protein will be transformed into the active state thus will respond to the excitation/bleaching laser, thus irradiates light and becomes bleached after prolonged excitation. The process is repeated until adequate amount of data is acquired. Single molecule localization is performed for each data set where single emitters can be identified, and the localization result will be overlaid together to yield the final PALM image.
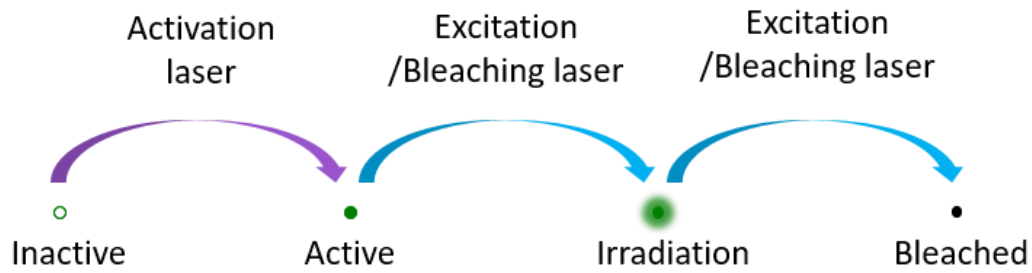
Figure 1.2. Property of Photoactivable Fluorescence Proteins (FA-FPs).

As illustrated above, the FA-FPs can be activated by the activation laser, and be excited by the excitation/bleaching laser to turn into irradiation state (bright). Prolonged excitation will further term the fluorescence protein into bleached state.
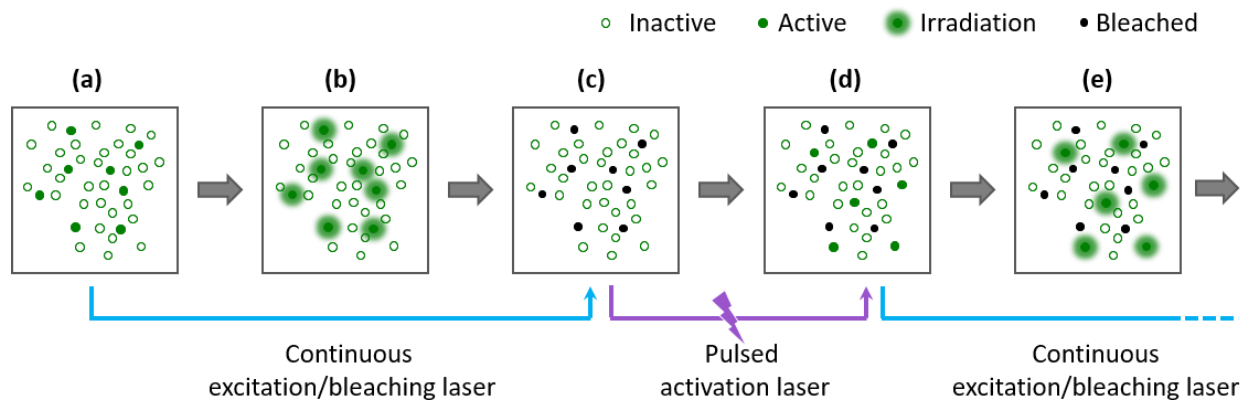
Figure 1.3. Data acquisition of Photo-activated localization microscopy (PALM).

At the initial imaging state, only a small portion of the FA-FPs are in the active state as shown in

(a). Only the active fluorescence proteins will response to the excitation/bleaching laser and turns

into irradiation state as shown in (b). Prolonged excitation of the activate FP will transform them

into the bleached state as shown in (c). A pulsed activation laser can activate another portion of

the inactive FA-FPs and turn them into active state as shown in (d). Then the next cycle begins by

continuous excitation/bleaching laser so the activated FPs will now response and irradiate light, as

shown in (e). The cycle goes back to panel (c) and repeat until adequate amount of data is acquired.

Stochastic Optical Reconstruction Microscopy (STORM)

Stochastic optical reconstruction microscopy(STORM) was developed by Xiaowei Zhuang, et al. [1.3] in 2006. Instead of using photoactivable fluorescence proteins, STORM utilizes the photo switchable dyes to achieve blinking control in the fluorophores thus to achieve the active fluorophore density condition for single molecule localization at given time instance. The practice of STORM also takes advantage of the different response of photo switchable dyes to two different lasers, as illustrated in Figure 1.4. One laser is responsible for the excitation of the fluorophore as well as switching the fluorophore into a non-radiative dark state. Another laser is responsible for switching the fluorophores in the dark state back into the fluorescent state. Such dye such as Cy5 can be switched on and off for hundreds of cycles before it is photo-bleached, allowing multiple appearance of the same single molecule over the acquisition series. Over the past years, a family of different photo-switchable fluorophores has been engineered and discovered that possess different photo switching properties with different emission wavelength [1.8], allowing for multi-color STORM image and many advances of STORM technique.
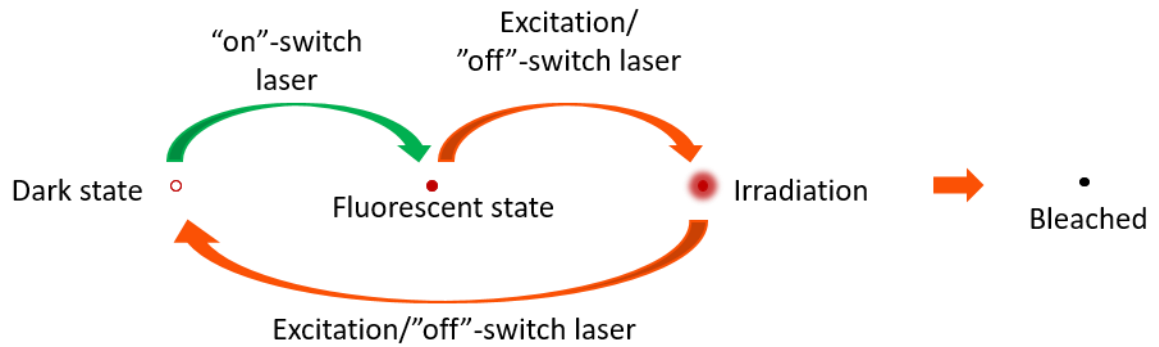
Figure 1.4. Property of photo-switchable dyes.

Photo-switchable dyes can be switched between the dark state and fluorescent state. The dark state dye can be switched 'on' by a "on"-switch laser into the fluorescent state. When a dye is in fluorescence state, it can response to the excitation/"off"- switch laser that either drives the dye to irradiate light or switch it back into the dark state. One single dye can be switched between "on" and "off" for multiple cycles before it turns into the bleached state.
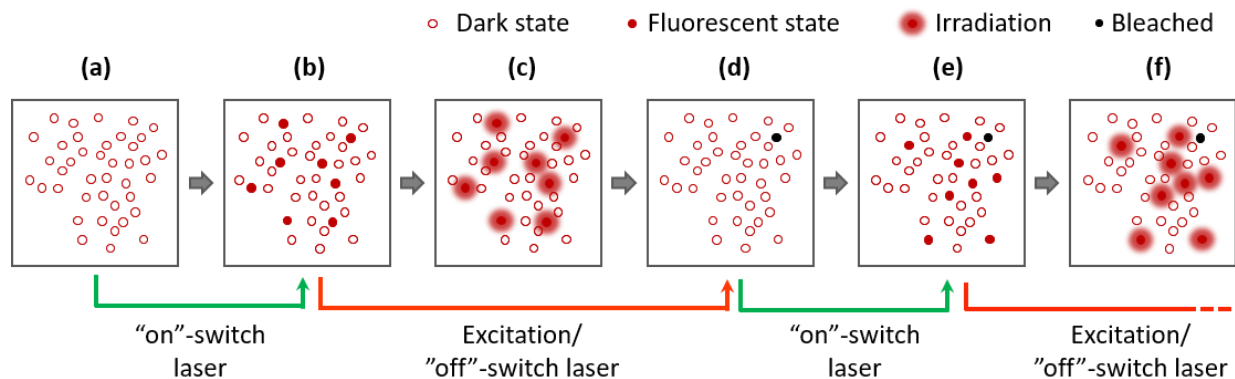
Figure 1.5. Data acquisition of Stochastic Optical Reconstruction Microscopy (STORM).

In the practice of STORM, all the dyes are turned into the "dark" state at the beginning as shown in (a), then a short illumination of the "on"-switch laser is turned on where a small portion of the dye will be switched to the fluorescence as shown in (b). Fluorescence state dyes will irradiate light under excitation laser as shown in (c), and can be further switched into the dark state at the same time as shown in (d). Then the next cycle begins by a short illumination of the "on"-switch laser as shown in (d) that corresponds to (a), another portion of the dyes will be switched to the fluorescent state as shown in (e) in accordance with (b), then under the illumination of excitation laser the new portion of the dyes in fluorescent state will irradiate light. During the data acquisition, all the images that shows small portion of fluorophores as bright molecules will be analyzed where single molecule localization are performed for each identified single fluorophores, to construct for the final super-resolution image.

1.3.   Stimulated Emission Depletion (STED) microscopy

Stimulated emission depletion (STED) microscopy is a scanning based super-resolution technology where the excitation beam is co-centered with a doughnut shape de-excitation beam (STED beam) to confine the spontaneous fluoescence area in to a focal spot below the size of diffraction limit thus to achieve super-resolution [1.4]. The principal of STED relies greatly on the difference between spontaneous emission and stimulated emission, as illustrated in panel (a) of Figure. 1.6, where the energy levels are depicted for a typical fluorophore. After the fluorophore is excited from ground state (G) to the excitation state (E), as shown in Figure 1.6 (a) as transition from L_0 to L_1, the fluorophore can transit from L_1 into L_2 state, from which the fluorophore further transit into the ground state and emit a photon. This emission process is called spontaneous emission with the absence of external field and the lifetime of L_2 is typically 2 ns [1.4]. When there exist an external optical field that matches the energy difference between the energy states L2 and L3, the transition rate from L_2 to L_3 will be greatly increased, this emission process is called stimulated emission. The practice of STED (Figure 1.7) takes uses a focused excitation laser to transform the emitters from ground state into the excited state(Figure 1.7(a) to (c)), and a doughnut shape STED beam that is co-centered with the excitation beam is applied (Figure 1.7(d)) before simultaneous fluorescence take place. The STED beam will deplete the excited emitters (Figure 1.7(e)) in the area covered by the STED beam, such that only the center part of the STED beam will undergo spontaneous fluorescence (f). The spontaneous fluorescence signal is collected and will form one pixel in the STED image, where the location of this pixel is determined by the center of the excitation beam and STED beam. Scanning the excitation beam and STED beam across the entire field of view allows the reconstruction of the image with the resolution defined by the non-

depleted region of the STED beam, which is much smaller than the diffraction limited excitation beam, thus yield the reconstructed STED image with super-resolution.
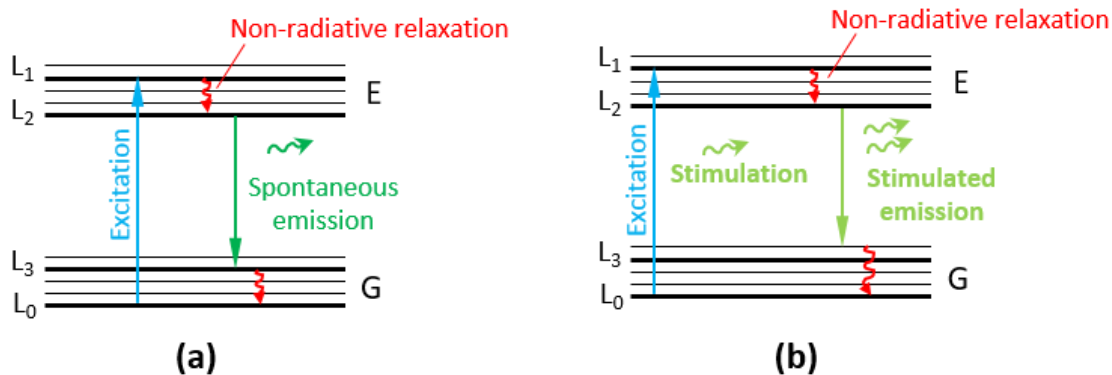
Figure 1.6. Energy diagram of a fluorophore with different fluorescence mechanism.
When The fluorophore is excited from the ground state (G) to the excited state (E), as illustrated in both **(a)** and **(b)**, the fluorophore can undergo spontaneous fluorescence as shown in **(a)** without the existence of an external optical field. And at the presence of an optical field that is on resonance with a certain energy difference between an excitation state and a ground state, the fluorophore will undergo stimulated fluorescence as shown in **(b)**. In the case of spontaneous fluorescence, the lifetime of L_2 is around 2 ns, however under the case of stimulated fluorescence the lifetime is much faster, creating a time difference between the two different type of fluorescence signals. In addition, the wavelength of the emitted photons from the two different types of fluorescence signal are different, allowing the selective collection of spontaneous fluorescence signal.
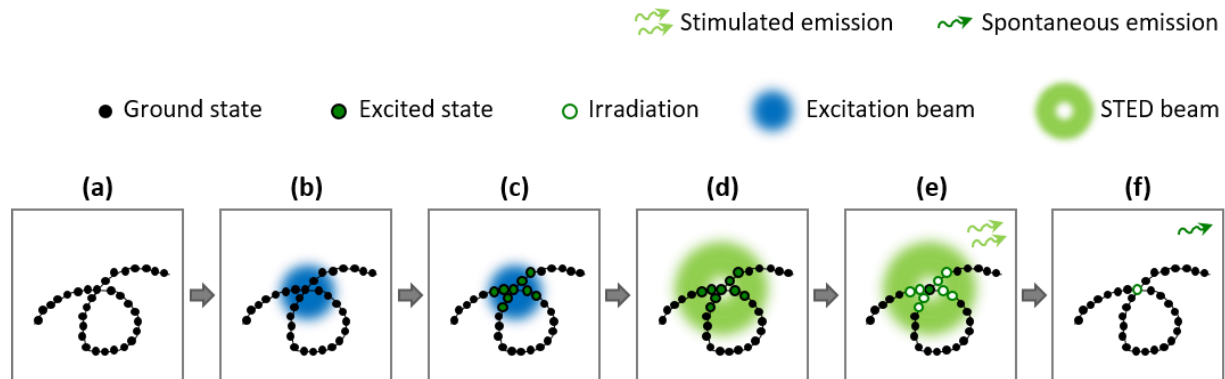
Figure 1.7. Stimulated Emission Depletion (STED) microscopy.

In the practice of STED, each individual pixel of the STED image is constructed with the cycle explained in this figure. (a) shows the feature of interest labeled with fluorophores, excitation beam is applied as shown in (b) that transit the fluorophores within the excited volume into the excited state as shown in (c). Right after the excitation beam is applied and before spontaneous emission takes place, a doughnut shape STED beam (co-centered with the excitation beam) is applied as shown in (d) and causes most of the fluorophores undergo stimulated emission thus depleted from the excited state as shown in (e). The fluorophores located at the center region of the STED beam will not be stimulated thus can have spontaneous emission as shown in (f). The spontaneous fluorescence emission is collected to form a pixel in the STED image at the location of the center of the excitation beam and STED beam. The same process is repeated by scanning the beams across the field of view to achieve the final STED image reconstruction.

1.4.   Structured illumination Microscopy (SIM)

In the conventional fluorescence microscope, the spectrum of feature of interest is truncated by the aperture of the optical system, resulting in the diffraction limited image observation with limited resolution. Structured illumination Microscopy utilizes structured illumination to encode high frequency component in the Fourier plane that is otherwise not available due to limited numerical aperture of the optical system. Super-resolution is achieved with the high frequency information encoded by the structured illumination pattern as shown in Figure 1.8. In the conventional sense, SIM uses sinusoidal patterned illuminations for excitation as shown in Figure 1.8(b). Given the fact that the fluorescence intensity is linearly dependent on the excitation field intensity, the image brightness is the product of the excitation pattern and the image of the feature of interest (Figure 1.8(c)). This means in the frequency domain which is the Fourier transform of the image, the spectrum will be the convolution of the original frequency spectrum for the feature of interest (Figure 1.8(d)), and the spectrum of the illumination field (Figure 1.8(e)). The spectrum of the sinusoidal illumination pattern is three delta peaks with one peak located at the origin point in the Fourier space, and two peaks located symmetrically away from the origin point. So the convolution of the two spectrum will yield three overlapping duplicates of the spectrum of the feature of interest as shown in Figure 1.8(f) and illustrated in Figure 1.8(g)(h)(i)(j). Due to the limited aperture size of the optical system, the frequency components that are collected in the image is only the center part that passes the pupil function. Due to the sinusoidal illumination field, information of the high frequency component regime of the original image spectrum is shifted to be within the aperture of the system, as shown in Figure 1.8(j) that can be solved and shifted back to the corresponding regime as shown in Figure 1.8(k). Repeating the process for many different

sinusoidal illumination patter to extend the frequency domain as shown in Figure 1.8(l), inverse Fourier transform of the extended spectrum will yield SIM image reconstruction with enhanced resolution. Figure 1.9 illustrate the big picture of SIM reconstruction, where the original image spectrum (Figure 1.9(a) and (d)) is truncated by the aperture of the optical system (Figure 1.9(e)) that yields the diffraction limited image as shown in Figure 1.9(b), and with SIM reconstruction, the high frequency domain of the image spectrum can be recovered (Figure 1.9(f)) to yield SIM image reconstruction with 2 fold resolution enhancement (Figure 1.9(c)).
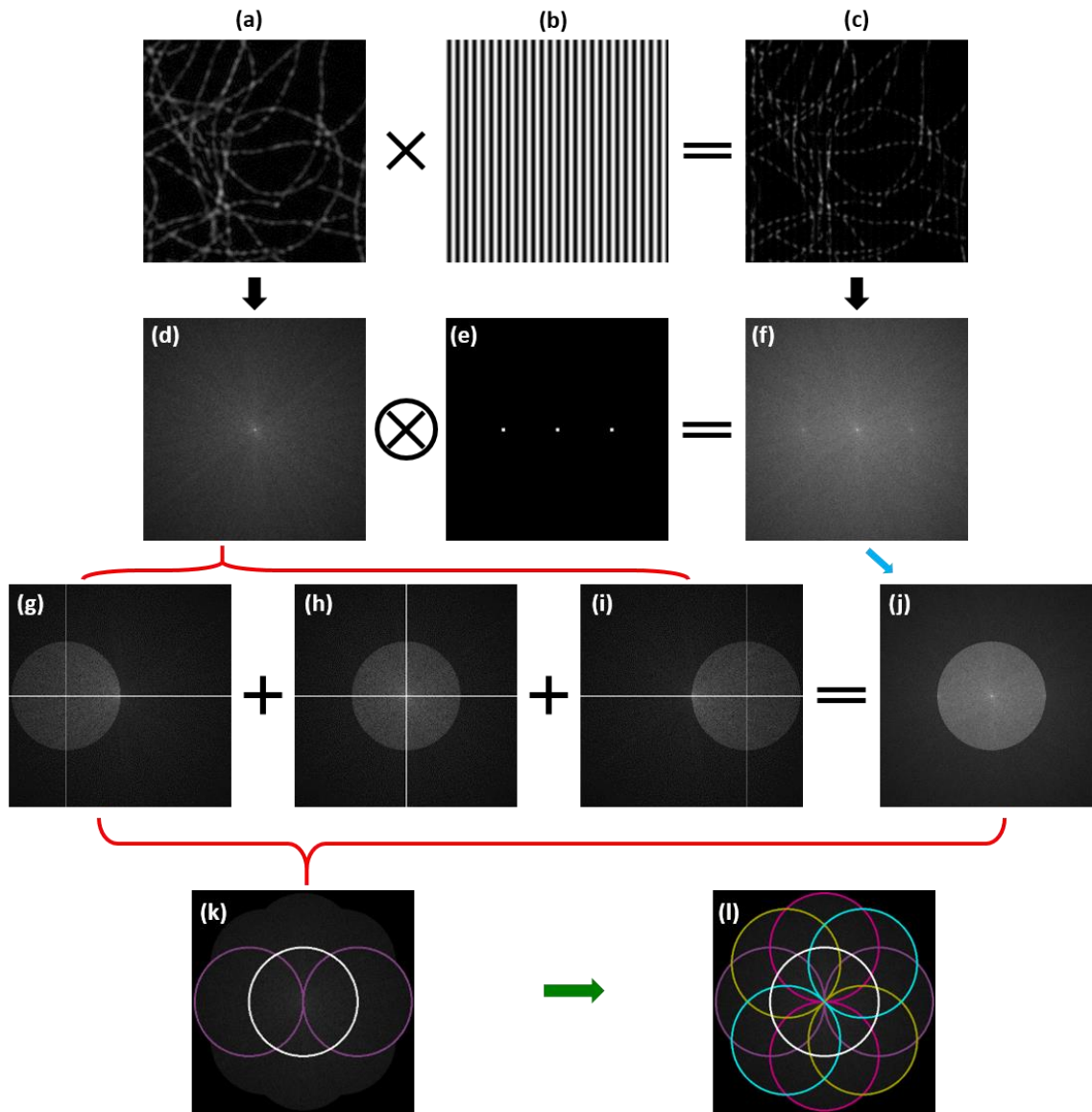
Figure 1.8. Principals of Structured Illumination Microscopy.

(a) shows the original labeled feature of interest. (b) shows one sinusoidal illumination pattern as an example. (c) the captured image would be the product between the illumination pattern and the original labeled feature of interest (diffraction limited). (d) shows the spectrum of the original feature of interest, (e) shows the spectrum of the illumination patter, and (f) shows the spectrum of the image under such illumination patter. We can see that the spectrum is actually the

17

convolution between the spectrums of the original feature of interest and the spectrum of the illumination patter. The captured image is actually from the spectrum truncated by the aperture as shown in (j), and can be decomposed as three components centered at different locations from the spectrum of the original feature of interest as shown in (g)(h)(i). Shifting the phase of the sinusoidal illumination pattern allow us to solve for the three components shown in (g)(h) and (i), that can be shifted back and extend the observed spectrum as shown in (k). Repeat the process with sinusoidal illumination patter with different orientation will results in the spectrum extension in multiple directions as shown in (l).
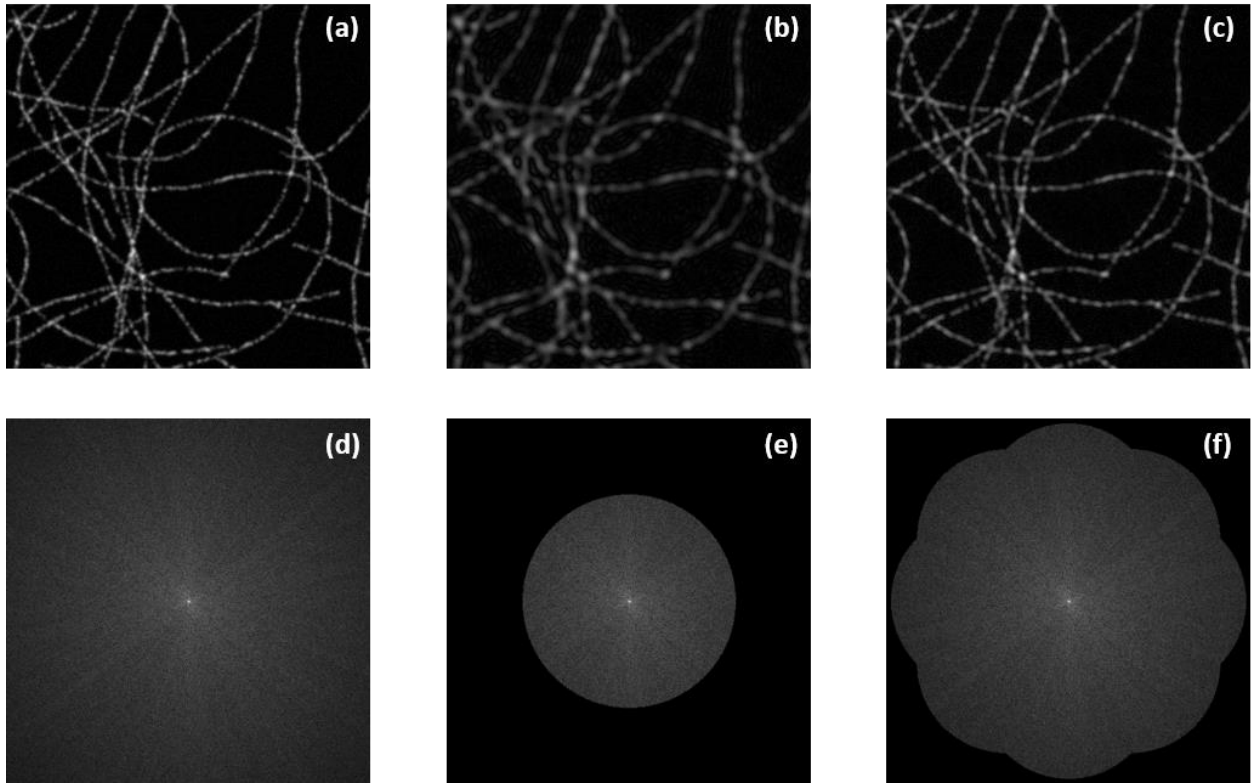
Figure 1.9. Resolution enhancement of Structured Illumination Microscopy.

Given the feature of interest as shown in (a), the spectrum of the image is shown in (d).

However, the observed image (b) is diffraction limited and the spectrum of the image is

truncated by the aperture of the optical system. SIM image reconstruction (c) process enhanced

resolution that is below the diffraction limit because of the extended spectrum as shown in (f).

1.5. References

[1.1]. S. G. Lipson, H. Lipson and D. S. Tannhauser. 1998. Optial Physics. Page 340.

[1.2]. E. Betzig, et al. 2006. Imaging intracellular fluorescent proteins at nanometer resolution. Science 313.5793: 1642-1645.

[1.3]. M. J. Rust, M. Bates, X. Zhuang. 2006. Sub-diffraction-limit imaging by stochastic optical reconstruction microscopy (STORM). Nature methods 3.10 (2006): 793-796.

[1.4]. S. W. Hell, J. Wichmann, 1994. Breaking the diffraction resolution limit by stimulated emission: Stimulated-emission-depletion fluorescence microscopy. Optics Letter. 19(11):780-782.

[1.5]. M. GL. Gustafsson. 1999. Extended resolution fluorescence microscopy. Current opinions in structural biology 9.5: 627-634.

[1.6]. M. GL. Gustafsson. 2000. Surpassing the lateral resolution limit by a factor of two using structured illumination microscopy. Journal of microscopy: 198.2:82-87.

[1.7]. R. Heintzmann, C. G. Cremer. 1999. Lateral modulated excitation microscopy: Improvement of resolution by using a diffraction grating. Proc. SPIE 356: 185-196.

[1.8]. K Xu, G Zhong, X Zhuang. 2013. Actin, spectrin, and associated proteins form a periodic cytoskeletal structure in axons. Science 339.6118: 452-456.

Chapter 2. A review of SOFI theory

2.1.   General review of SOFI

SOFI relies on the stochastic fluctuations of optical signal introduced under variety of occasions. Such as the stochastic blinking of emitters demonstrated in the existing SOFI works [2.1], or other types of optical fluctuation demonstrated in multiple SOFI derivatives including diffusion of particles [2.2], FRET due to diffusion [2.3], or induced from stochastic speckle illumination [2.4].

The theoretical resolution enhancement for SOFI at n[th] order is $\sqrt{n}$ fold. Once combined with deconvolution or Fourier re-weighting [2.5], this enhancement becomes n-fold. Because of this continuous resolution enhancement with the increase of SOFI order, it is of particular interest to seek for high order SOFI applications. In practice, the fundamental issues that limit the application of high order SOFI includes the non-linear expansion of pixel intensity dynamic range, and cusp-artifacts (will be discussed in Chapter 3).

2.2.   SOFI algorithm implementation

In the practice of SOFI, the sample is labeled with emitters possess stochastic blinking behavior. Such labeled sample is imaged under fluorescence microscopy where consecutive frames are recorded and processed to yield SOFI image. Given a sample with N emitters that blink independently, the fluorescence signal captured at location $\vec{r}$ and time t is characterized as follows:

$$F(\vec{r},r) = \sum_{k=1}^{N} \epsilon_k \cdot b_k(t) \cdot U(\vec{r}-\vec{r}_k) \tag{2.1}$$

where k is the index of emitter, ϵ_k is the 'on'-state brightness of the kth emitter, $b_k(t)$ is the

time dependent blinking profile of kth emitter where we have:

$$b_k(t) = \begin{cases} 1, & \text{when emitter is at 'on'-state} \\ 0, & \text{when emitter is at 'off'-state} \end{cases} \tag{2.2}$$

$U(\vec{r})$ is the point spread function (PSF) of the current imaging system, and $\vec{r}_k$ is the location of

the kth emitter. In SOFI calculation, we first take the raw data with T total frames, and calculate

the time average of each pixel as follows:

$$\langle F(\vec{r},t) \rangle_t = \frac{1}{T} \sum_{t=1}^{T} F(\vec{r},t) \tag{2.3}$$

We subtract the time average $\langle F(\vec{r},t) \rangle_t$ from $F(\vec{r},t)$ as follows:

$$\delta F(\vec{r},t) = F(\vec{r},t) - \langle F(\vec{r},t) \rangle_t \tag{2.4}$$

and obtain $\delta F(\vec{r},t)$ as the fluctuation of $F(\vec{r},t)$.

Then we can calculate the autocorrelation functions of $\delta F(\vec{r},t)$ along the time axis with time lags

$(\tau_1, \tau_2, ..., \tau_n)$ at order n as follows:

$$G_n(\vec{r}, \tau_1, \tau_2, ..., \tau_n) = \langle \delta F(\vec{r}, t+\tau_1) \cdot \delta F(\vec{r}, t+\tau_2) \cdots \delta F(\vec{r}, t+\tau_n) \rangle_t \tag{2.5}$$

Usually the first time lag τ_1 is set to 0. Cross-correlation functions with $\delta F(\vec{r},t)$ from different

pixel locations (different $\vec{r}$ values) can also be calculated:

$$G_n(\vec{r}_1, \vec{r}_2, ..., \vec{r}_n; \tau_1, \tau_2, ..., \tau_n) = \langle \delta F(\vec{r}_1, t) \cdot \delta F(\vec{r}_2, t+\tau_1) \cdots \delta F(\vec{r}_n, t+\tau_n) \rangle_t \tag{2.6}$$

Replace $\delta F(\vec{r}_i, \tau_i)$ with notation δF_i , equation (2.6) is simplified as:

$$G_n(\delta F_1, \delta F_2,...,\delta F_n) = \left\langle \delta F_1 \cdot \delta F_2 \cdots \delta F_n \right\rangle_t \qquad (2.7)$$

We address $G_n(\delta F_1, \delta F_2,...,\delta F_n)$ as the joint correlation function for set $\{\delta F_i \mid i \in [1,n]\}$, which is defined by the choice of pixel combinations and time lags combinations. For a given instance of time lags $\{\tau_1, \tau_2,...,\tau_n\}$, we also address $G_n(\delta F_1, \delta F_2,...,\delta F_n)$ as the **joint-moment** of set $\{\delta F_i \mid i \in [1,n]\}$.

The next step is to calculate the nth order cumulant, denoted as $C_n(\delta F_1, \delta F_2,...,\delta F_n)$ which we address as **joint-cumulant** of set $\{\delta F_i \mid i \in [1,n]\}$. Note that a special case of equation (2.6) with $\vec{r} = \vec{r}_1 = \vec{r}_2 = ... = \vec{r}_n$ reduces to equation (2.5), consequently, the differences between auto-correlation functions and cross-correlation functions are retained while we form our discussion under the framework of joint-moments and joint-cumulants in the general sense.

(a)

$$\delta F(\vec{r_1},\tau_1)\quad \delta F(\vec{r_2},\tau_2)\quad \delta F(\vec{r_3},\tau_3)\quad \delta F(\vec{r_4},\tau_4)\quad \delta F(\vec{r_5},\tau_5)$$

(A) δF_A — (B) δF_B — (C) δF_C — (D) δF_D — (E) δF_E

Set of 5 element

(b)

Number of parts (q)	Size of parts $\{s_1,s_2,...,s_q\}$	All partitions	(f_1) $(-1)^{q-1}(q-1)!$	(f_2) of the circled partition	circled partition
1	$\{5\}$		$(-1)^{1-1}(1-1)!$ $=1$	$\langle \delta F_A\,\delta F_B\,\delta F_C\,\delta F_D\,\delta F_E\rangle_t$	
2	$\{3,2\}$		$(-1)^{2-1}(2-1)!$ $=-1$	$\langle \delta F_A\,\delta F_B\,\delta F_D\rangle_t\cdot\langle\delta F_C\,\delta F_E\rangle_t$	
	$\{4,1\}$		$(-1)^{2-1}(2-1)!$ $=-1$	$\langle \delta F_A\,\delta F_B\,\delta F_C\,\delta F_E\rangle_t\cdot\langle\delta F_D\rangle_t$	
3	$\{3,1,1\}$		$(-1)^{3-1}(3-1)!$ $=2$	$\langle \delta F_A\,\delta F_B\,\delta F_D\rangle_t$ $\cdot\langle\delta F_C\rangle_t\cdot\langle\delta F_E\rangle_t$	
	$\{2,2,1\}$		$(-1)^{3-1}(3-1)!$ $=2$	$\langle \delta F_A\,\delta F_B\rangle_t\cdot\langle\delta F_C\rangle_t$ $\cdot\langle\delta F_D\,\delta F_E\rangle_t$	
4	$\{2,1,1,1\}$		$(-1)^{4-1}(4-1)!$ $=-6$	$\langle \delta F_A\,\delta F_B\rangle_t\cdot\langle\delta F_C\rangle_t$ $\cdot\langle\delta F_D\rangle_t\cdot\langle\delta F_E\rangle_t$	
5	$\{1,1,1,1,1\}$		$(-1)^{5-1}(5-1)!$ $=24$	$\langle \delta F_A\rangle_t\cdot\langle\delta F_B\rangle_t\cdot\langle\delta F_C\rangle_t$ $\cdot\langle\delta F_D\rangle_t\cdot\langle\delta F_E\rangle_t$	

Figure 2.1. Calculation of 5th order joint-cumulant.

A set of five elements is shown in **(a)**, where the element is the fluctuation profile of five pixels.

Repeating pixels are allowed, for example if element A and B are repeating pixels, we have $\vec{r_1}=\vec{r_2}$

. Simplified notations for the five elements are $\{\delta F_A,\delta F_B,\delta F_C,\delta F_D,\delta F_E\}$ respectively. **(b)**

demonstrate all possible partitions of a set of five elements, and how each partition contributes a

24

term to the summation series (as the product of f_1 and f_2) to yield the joint-cumulant. Note here that all the partitions that contain a part of size 1 equals to 0, because $\langle \delta F(t) \rangle_t = 0$. The graphical demonstration of partitions are inspired by the work by Tilman Piesk [2.6]

The calculation of joint-cumulant of set $\{\delta F_i \mid i \in [1, n]\}$ is illustrated in Figure 2.1 in the case of 5th order as an example. In the general sense regardless of the choices of $\{\delta F_i \mid i \in [1, n]\}$, n fluorescence fluctuations profiles are selected from individual pixels (with or without pixel repetition) to form the set $\{\delta F_i \mid i \in [1, n]\}$ (Figure 2.1(a)), from which all the possible partitions are identified as shown in Figure 2.1(b). Partitions can possess different number of parts where each parts can possess different number of element (1st and 2nd columns in Figure 2.1(b)). For each partition, the elements of set $\{\delta F_i \mid i \in [1, n]\}$ are grouped into specific parts as subsets of $\{\delta F_i \mid i \in [1, n]\}$), where each part is a subset of $\{\delta F_i \mid i \in [1, n]\}$ (3rd column in Figure 2.1(b)). Each specific partition of set $\{\delta F_i \mid i \in [1, n]\}$ contributes one term to a summation series to construct the joint-cumulant, where each term can be expressed as the product of two factors, as shown in the 4th- and 5th column in Figure 2.1(b). The first factor (f_1) depends on the size of this partition (denote as q in 1st column in Figure 2.1(b)) and is defined as: $(-1)^{q-1}(q-1)!$ (4th column in Figure 2.1(**b**)), the second factor (f_2) is the product of all the joint-moments of each part within this partition: if we use I to represent for set $\{\delta F_i \mid i \in [1, n]\}$, and I_p (with $p = 1, 2, 3, ..., q$) to represent for different parts that belongs to this partition (as different subsets of I), we have $I_1 \cup I_2 \cup ... \cup I_q = I$. The joint-moments for each part I_p (denote as $G(I_p)$) are multiplied together to yield $G(I_1) \cdot G(I_2) \cdots G(I_q)$ as the second factor (f_2), as illustrated in the 5th column in Figure 2.1(**b**).

In conclusion, given a set of intensity trajectories as a group of pixels (set I), either with or without

26

pixel repetition, the joint-cumulant of I is constructed as a function of joint-moments of all the parts over all possible partitions of set I based on the following formula[1]:

$$C_n(I) = \sum_{\substack{\text{all partitions of I:} \\ I_1 \cup I_2 \cup ... \cup I_q = I}} (-1)^{q-1}(q-1)!\, G(I_1) \cdot G(I_2) \cdots G(I_q)$$

(2.8)

Note here that in equation (2.8) the joint-moments $G(I_p)$ are essentially the lower order correlation functions discussed in the original SOFI paper[2.1]. If a partition contains a part that has only one element, we have the corresponding $G(I_p)$ as $\langle \delta F(t) \rangle_t = 0$, so the corresponding f_2 factor will be 0, thus this partition will not contribute to the joint-cumulant calculation. The actual partitions that have a contribution to the joint-cumulant are those without any parts that contains only one element, the case of 5th order is shown Figure 2.2.

(a)

Set of 5 element
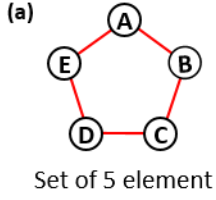
(b)

Number of parts (q)	(f_1) $f_1=(-1)^{q-1}(q-1)!$	(f_2) factors for different partitions		
1	$(-1)^{1-1}(1-1)!=1$	$\langle \delta F_A\, \delta F_B\, \delta F_C\, \delta F_D\, \delta F_E \rangle_t$		
2	$(-1)^{2-1}(2-1)!=-1$	$\langle \delta F_A\, \delta F_D\, \delta F_E \rangle_t \cdot \langle \delta F_B\, \delta F_C \rangle_t$		$\langle \delta F_A\, \delta F_C\, \delta F_D \rangle_t \cdot \langle \delta F_B\, \delta F_E \rangle_t$
		$\langle \delta F_C\, \delta F_D\, \delta F_E \rangle_t \cdot \langle \delta F_A\, \delta F_B \rangle_t$		$\langle \delta F_B\, \delta F_C\, \delta F_E \rangle_t \cdot \langle \delta F_A\, \delta F_D \rangle_t$
		$\langle \delta F_B\, \delta F_C\, \delta F_D \rangle_t \cdot \langle \delta F_A\, \delta F_E \rangle_t$		$\langle \delta F_A\, \delta F_B\, \delta F_D \rangle_t \cdot \langle \delta F_C\, \delta F_E \rangle_t$
		$\langle \delta F_A\, \delta F_B\, \delta F_C \rangle_t \cdot \langle \delta F_D\, \delta F_E \rangle_t$		$\langle \delta F_A\, \delta F_C\, \delta F_E \rangle_t \cdot \langle \delta F_D\, \delta F_B \rangle_t$
		$\langle \delta F_A\, \delta F_B\, \delta F_E \rangle_t \cdot \langle \delta F_C\, \delta F_D \rangle_t$		$\langle \delta F_B\, \delta F_D\, \delta F_E \rangle_t \cdot \langle \delta F_A\, \delta F_C \rangle_t$

(c)

$$C_5(\delta F_A, \delta F_B, \delta F_C, \delta F_D, \delta F_E) = \langle \delta F_A\, \delta F_B\, \delta F_C\, \delta F_D\, \delta F_E \rangle_t$$
$$-\langle \delta F_A\, \delta F_D\, \delta F_E \rangle_t \cdot \langle \delta F_B\, \delta F_C \rangle_t - \langle \delta F_A\, \delta F_C\, \delta F_D \rangle_t \cdot \langle \delta F_B\, \delta F_E \rangle_t$$
$$-\langle \delta F_C\, \delta F_D\, \delta F_E \rangle_t \cdot \langle \delta F_A\, \delta F_B \rangle_t - \langle \delta F_B\, \delta F_C\, \delta F_E \rangle_t \cdot \langle \delta F_A\, \delta F_D \rangle_t$$
$$-\langle \delta F_B\, \delta F_C\, \delta F_D \rangle_t \cdot \langle \delta F_A\, \delta F_E \rangle_t - \langle \delta F_A\, \delta F_B\, \delta F_D \rangle_t \cdot \langle \delta F_C\, \delta F_E \rangle_t$$
$$-\langle \delta F_A\, \delta F_B\, \delta F_C \rangle_t \cdot \langle \delta F_D\, \delta F_E \rangle_t - \langle \delta F_A\, \delta F_C\, \delta F_E \rangle_t \cdot \langle \delta F_D\, \delta F_B \rangle_t$$
$$-\langle \delta F_A\, \delta F_B\, \delta F_E \rangle_t \cdot \langle \delta F_C\, \delta F_D \rangle_t - \langle \delta F_B\, \delta F_D\, \delta F_E \rangle_t \cdot \langle \delta F_A\, \delta F_C \rangle_t$$

Figure 2.2. Analytical expression of 5th order joint-cumulant.

(a) shows a set with five elements as shown in figure 2.1. **(b)** shows the effective partitions that possess contributions to the joint-cumulant. **(c)** shows the analytical form of this joing-cumulant expressed as a function of individual fluorescence fluctuation profiles δF_x.

2.3.   Physical meaning of SOFI cumulant

It is worth to be noticed here that the choices of the pixels to form the joint-cumulant can all be the same pixel repeated for n times in the case of nth order, or from different pixels with partial repeating pixels, or without repeating pixels. The location of the SOFI pixel would be the geometry center of all the pixels in the pixel combination, which gives rise to the ability of achieving virtual pixels at locations that original doesn't have a real pixel. This capability allows for extra sampling frequency of the image as required by the increased spatial resolution as the SOFI order increases.

In order to understand the physical meaning of SOFI cumulant, we suubstitute equation (2.1) - (2.7) into equation (2.8) we find the expression of nth order joint-cumulant of set $\{\delta F(\vec{r}_i, \tau_i) \mid i \in [1,n]\}$ as follows:

$$
\begin{aligned}
&C_n(\vec{r}_1, \vec{r}_2, ..., \vec{r}_n; \tau_1, \tau_2, ..., \tau_n) \\
&= W_n(\vec{r}_1, \vec{r}_2, ..., \vec{r}_n) \cdot \sum_{k=1}^{N} \epsilon_k^n C_n\left(\delta b_k(t+\tau_1), \delta b_k(t+\tau_2), ..., \delta b_k(t+\tau_n)\right) \cdot U^n(\vec{r}_{gc} - \vec{r}_k) \\
&\text{with:} \\
&W(\vec{r}_1, \vec{r}_2, ..., \vec{r}_n) = \prod_{\substack{i \in [1,n] \\ j \in [1,n]}}^{i<j} U\left(\frac{\vec{r}_i - \vec{r}_j}{\sqrt{n}}\right)
\end{aligned}
\tag{2.9}
$$

Where $W_n(\vec{r}_1, \vec{r}_2, ..., \vec{r}_n)$ is the distance factor.

The SOFI pixel location is equivalence to the location of the geometry center of the selected pixels. The choice if pixel combination imposes a trade-off between noise contribution and the distance factor. When the distribution of the selected pixels is too far away, the distance factor will become

29

small thus attenuates the correlation signal. If we want to seek for a pixel combination that yield less attenuation imposed by the distance factor, at high orders we need to have repetition of pixels in the pixel combination. In my approach we went into the opposite extreme of this trade off, where we want to diminish the effect of distance factor at the sacrifice of noise contribution. Because noise can be expressed as another random variable so the contribution of noise is an additive term to the cumulant reconstruction and can be cleared out after fitting for the distance factor. We explain below our strategy of pixel combinations for high order SOFI pixels.
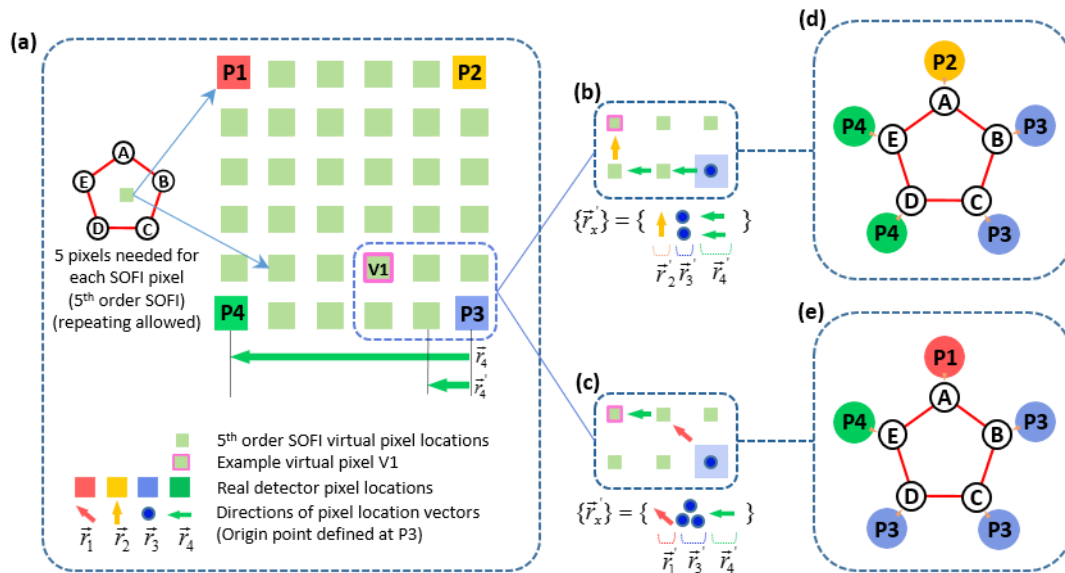
Figure 2.3. The choice of Pixel combination.

(a) shows a pixel array with {P1, P2, P3, P4} indicate real detector pixels and small green tiles indicate virtual pixel locations. {r1, r2, r3, r4} indicates the directions of real detector pixel location vectors while setting P3 as the origin point. **(b)** and **(c)** show two possible ways of choosing the real detector pixels such that the vector sum point at the indicated virtual pixel location V1. **(d)**

and **(e)** show shows the corresponding selection of pixel combinations respectively.

In the general sense, every SOFI pixel in the nth order SOFI image is calculated as the joint cumulant of a set of n elements (in the form of pixels with or without repetition) selected from a supply of real detector pixels. As indicated in Figure 3(a) (in the case of 5th order). As shown in Figure 2.3, we use the case of 5th order SOFI to explain how to choose the pixel combinations. We demonstrate here a pixel array with four real detector pixels {P1, P2, P3, P4} as the supply, and all possible virtual pixel locations corresponding to 5th order. Each virtual pixel requires the 5 element set {A, B, C, D, E} constructed with elements from the real pixel supply {P1, P2, P3, P4}, with allowance of repeating pixels. For a given SOFI pixel location, the choice of the five elements from the real pixel supply {P1, P2, P3, P4} need to carry their geometry center located at the SOFI pixel. The total number of pixel combinations that yield all the SOFI pixels is enormous. In this example, all the SOFI pixels listed in (a) can be constructed by the combination of the four given real pixels, and there are 4^5=1024 candidate combinations to choose from, if we increase the supply of real pixels this number further increases).

An efficient way to search for such pixel combinations could be guided by the geometric interpretation of the geometry center of vectors. We can define location vectors of each pixels in the set {A, B, C, D, E} as $\{\vec{r}_A, \vec{r}_B, \vec{r}_C, \vec{r}_D, \vec{r}_E\}$ respectively. So the geometry center of these five real pixel locations would be $\vec{r}_{gc} = (\vec{r}_A + \vec{r}_B + \vec{r}_C + \vec{r}_D + \vec{r}_E)/5$. If we denote $\vec{r}_x' = \vec{r}_x/5$ where x represents for A, B, C, D, E, the calculation of geometry center $\vec{r}_{gc}$ is equivalence to aligning all the vectors of set $\{\vec{r}_x'\}$ one after another (with any order) from any pre-defined origin point, so the ending point of the last vector would be the location pointed by vector $\vec{r}_{gc}$.

In our example here, each vector $\vec{r}_x$ and $\vec{r}_x'$ can have 4 different possibilities based on the choices

of real pixels, denote as $\vec{r}_i$ and $\vec{r}_i{'}$ with i represents for 1, 2, 3, 4. If we define the origin point at location of P3, we can get directions of the vectors of real pixels as shown in (a). Note here that we have $\vec{r}_3 = \vec{0}$, so both $\vec{r}_3$ and $\vec{r}_3{'}$ doesn't have a direction. The length of one location vector (with $\vec{r}_4$ shown as an example in (a)) is the distance of the pixel to the origin point (P3 in this example). The length of $\vec{r}_i{'}$ is one fifth of the original location vector (see $\vec{r}_4{'}$ as an example in (a)). The summation of the vectors $\{\vec{r}_i{'}\}$ in a geometric way are shown in (b), and (c) where two possible choices of pixel combinations are demonstrated that both yield virtual pixel V1 as labeled in (a) (b) (c). Based on the vectors used in the alignment, we can get the corresponding pixel combinations as shown in (d) and (e) respectively, where in (d) the set of five pixels is {P2, P3, P3, P4, P4}; and in (e) the set is {P1, P3, P3, P3, P4}. Note here that the repeating pixel P3 is zero vector, so the repeating $\vec{r}_3{'}$ is overlapping with each other in (b) and (c).

2.4.   Virtual-emitter interpretation of SOFI cumulants

In order to better understand and describe the physical meaning of SOFI cumulants discussed above, we want to introduce the virtual-emitter interpretation of SOFI cumulants. As discussed above, there are two major differences between the original image and nth order SOFI cumulant image (Equation 2.1 and 2.6). First, the PSF width is reduced by a factor of $\sqrt{n}$, we call the narrower PSF virtual PSF. Second, the brightness of kth emitter is characterized by $\epsilon_k b_k(t)$ in the original image, which is a time dependent intensity profile. In the nth order SOFI image, the apparent brightness of kth virtual emitter is $\epsilon_k w_{n,k}(\tau_1, \tau_2, ..., \tau_{n-1})$, we call it virtual brightness. Comparing the virtual brightness to the original brightness of the kth emitter, we can see that the first factor which contains the on-state brightness ϵ_k is raised to the power of n (becomes $\epsilon_k{}^n$),

33

this part contributes to the expanded brightness dynamic range of the resulting SOFI image. In addition, the second factor that carries the time dependent blinking profile $b_k(t)$ in the original image is changed into $w_{n,k}(\tau_1, \tau_2, ..., \tau_{n-1})$, which is the n$^{\text{th}}$ order cumulant of blinking profile fluctuation $\delta b_k(t)$. The location of emitters are not changed in SOFI cumulant image compared to the original image, we call these equivalence of emitters in the SOFI cumulant image virtual emitters.

The virtual-emitter interpretation of SOFI would thus be: For a given order of SOFI cumulant, the resulting image is equivalent to an image captured with a virtual microscope that has a virtual PSF with reduced width compared to the original PSF (thus increased resolution), and the captured signal is formed from virtual emitters that are located at exactly the same location as the real emitters in the imaging sample, but with virtual brightness's that differ from the real emitter brightness and could exhibit either positive or negative values.

2.5. References

[2.1]. T. Dertinger, R. Colyer, G. Lyer, S. Weiss. 2009. Fast, background-free, 3D super-resolution optical fluctuation imaging (SOFI). Proceedings of the National Academiy of Science. 106.52: 22287-22292.

[2.2]. L. Kisley, et al. 2015. Characterization of porous materials by fluorescence correlation spectroscopy super-resolution optical fluctuation imaging. ACS nano 9.9: 9158-9166.

[2.3]. S. Cho, et al. 2013. Simple super-resolution live-cell imaging based on diffusion-assisted Förster resonance energy transfer. Scientific reports 3:1208.

[2.4]. E. Hojman, et al. 2016. Photoacoustic imaging beyond the acoustic diffraction-limit with dynamic speckle illumination and sparse joint support recovery. arXiv preprint. arXiv: 1612.08278.

[2.5]. T. Dertinger, et al. 2010. Achieving increased resolution and more pixels with Superresolution Optical Fluctuation Imaging (SOFI). Optics express 18.18: 18875-18885.

[2.6]. https://en.wikipedia.org/wiki/Partition_of_a_set

Chapter 3.   Cusp artifacts of high order SOFI

In this chapter, we are going to talk about an intrinsic artifacts of high order SOFI cumulant, which we dub as Cusp artifact.

3.1.   Theoretical origin of cusp-artifact

As discussed in the 2nd chapter, the virtual brightness of virtual emitters in a high order SOFI image are dependent on the nth order cumulants of the blinking statistics of the corresponding real emitters in the sample. If we assume a two-state blinking profile $b_k(t)$ (k is emitter index) with $b_k(t) = 1$ indicates on-state, and $b_k(t) = 0$ indicates off-state, we can use ρ_k to represent for the percentage time that the emitter spent at on-state during the total data acquisition time. If the acquisition time is long enough such that the blinking behavior reaches statistical significance, for Poisson blinking, ρ_k would converge to $\tau_{on} / (\tau_{on} + \tau_{off})$, for pure power-law blinking statistics, ρ_k doesn't converge. Adjacent emitters can have different ρ_k values due to insignificant statistics during the acquisition time, or spatially subtle change of local microenvironment, or intrinsic property of the emitter type. Any order of Cumulant of $\delta b_k(t)$ can thus be expressed as a function of ρ_k. If we set all the time lags equal to zero, we find out that the cumulants with order higher than 2 will have positive-negative oscillations with the change of ρ_k. Given the nth order moments expressed as a function of ρ as follows:

$$M_n = \rho^n(1-\rho) + (1-\rho)^n(-\rho) \tag{3.1}$$

And with the interchangeable relation between cumulants and moments[3.1], we can have cummulants as functions of on-time ratio from 2nd order to 7th order are as follows:

$$\omega_2(\rho) = \rho - \rho^2$$
$$\omega_3(\rho) = \rho - 3\rho^2 + 2\rho^3$$
$$\omega_4(\rho) = \rho - 7\rho^2 + 12\rho^3 - 6\rho^4 \tag{3.2}$$
$$\omega_5(\rho) = \rho - 15\rho^2 + 50\rho^3 - 60\rho^4 + 14\rho^5$$
$$\omega_6(\rho) = \rho - 31\rho^2 + 180\rho^3 - 390\rho^4 + 360\rho^5 - 120\rho^6$$
$$\omega_7(\rho) = \rho - 63\rho^2 + 602\rho^3 - 2100\rho^4 + 3360\rho^5 - 2520\rho^6 + 720\rho^7$$

where emitter index k and the time lags $(\tau_1, \tau_2, ..., \tau_{n-1})$ are dropped to simplify the notation.

In Figure 3.1(v), we plot the different orders of cumulants as functions of "on"-time ratio we denote as ρ, we can clearly see the positive-negative oscillations of cumulants as functions of ρ at orders higher than 2nd order. In a high order SOFI image, if we have two virtual emitters located within the diffraction limit of the virtual PSF, it is possible that the virtual brightness of these two emitters have different ± values, as illustrated in Figure 3.1(i). The SOFI image, which shows the convolution of virtual emitters with the virtual PSF, will have a profile that has a positive lobe and a negative lobe. In the image display we usually take the amplitude of each pixel value, as illustrated in Figure 3.1(iv), the transition region becomes a cusp (so we call the resulting artifact cusp-artifact).
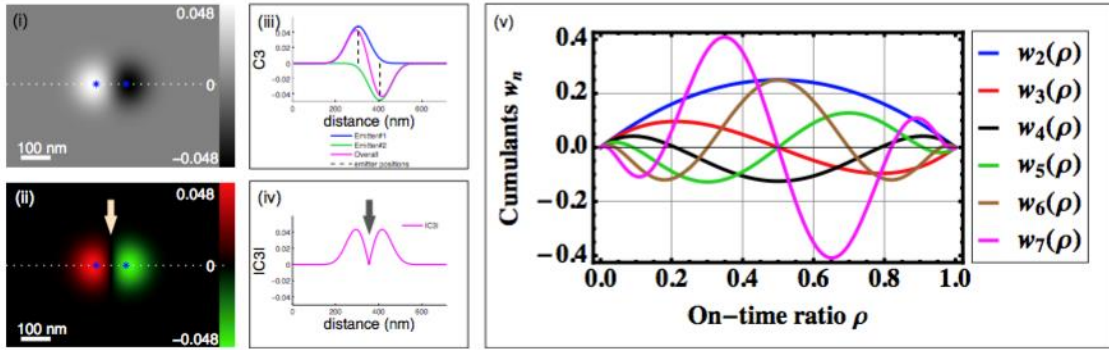
Figure 3.1. Conceptual demonstration of cusp artifact.

(i) and (ii) shows the theoretical 3rd order SOFI cumulant image of two emitters. The on-time ratio of left emitter is 0.4 for the left emitter, and 0.6 for the right emitter. (iii) and (iv) show the cross-section plot of the dashed line in (i) and (ii) respectively, where (iv) is the plot of absolute intensity value along the dashed line. (v) shows the plot of cumulants w_n as a function of ρ, with n = 2 to 7. We can see that when n > 2, w_n oscillates between negative and positive values under different manner with respect to the order n. In addition, we have $w_3(0.4) > 0$ and $w_3(0.6) < 0$, this corresponds to the virtual brightness shown in (i) and (ii), where the left emitter has positive virtual brightness and the right emitter has negative virtual brightness. So when we take the image display, we have cusp artifact indicated by the arrow in (ii) and (iv).

Order	2nd order	3rd order	4th order	5th order	6th order	7th order
Emitter 1/2/3 sign	+/+/+	−/+/+	+/−/+	+/−/−	−/+/−	+/+/−
SOFI	2.1e+04 ⋯ 3.8e+02	1.4e+06 ⋯ −2.1e+06	2.1e+08 ⋯ −6.3e+08	1.2e+11 ⋯ −1.3e+11	8.3e+13 ⋯ −6.1e+13	3.9e+16 ⋯ −9.8e+15
i	#1 #2 #3	#1 #2 #3	#1 #2 #3	#1 #2 #3	#1 #2 #3	#1 #2 #3
|i|	#1 #2 #3	#1 #2 #3	#1 #2 #3	#1 #2 #3	#1 #2 #3	#1 #2 #3
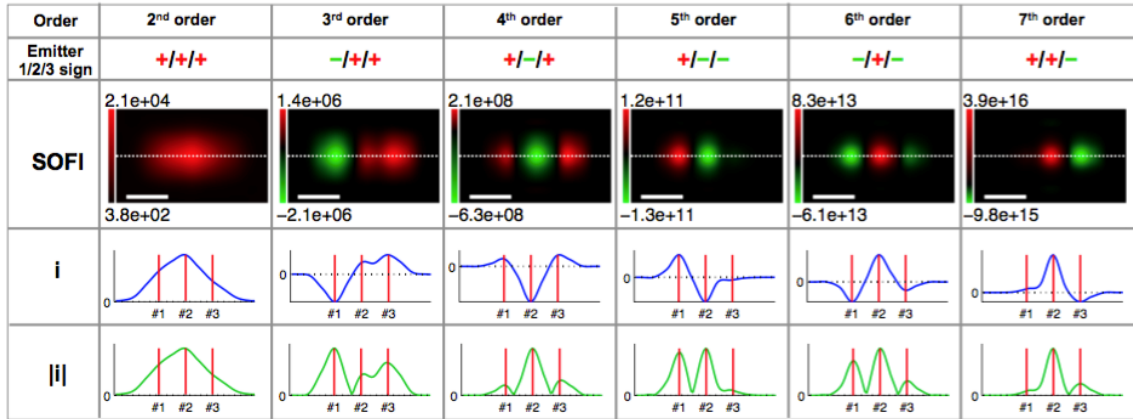
Figure 3.2. Cusps on blinking probes.

We here by performed realistic simulation of 3 emitters equally spaced with spacing distance 193 nm, the simulated emission wavelength is 800nm, with NA=1.4. Pixel size is 93.33 nm. For blinking statistics, we have ρ equal to 83.1%/41.6%/10.3% for emitter 1/2/3 respectively. The virtual brightness signs as predicted by Figure 3.1(v) of these three emitters is shown as (+/-) signs above each figure. SOFI images from left → right correspond to cumulant order 2,3,4,5,6,7. We can see that the virtual brightness signs follow the predictions. The dashed lines in each SOFI image are plot as i, and the absolute values are plot as |i|. We can clearly see the positive/negative oscillations in plots of i, and the cusps in the plots of |i|. Scale bars: 280nm.
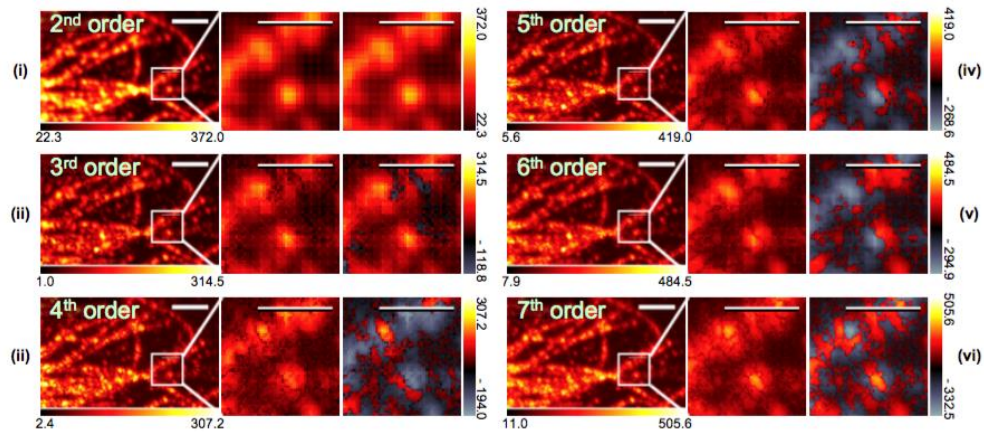
Figure 3.3. Cusp-artifact demonstration with experimental data.

We labeled fixed Hela cells with quantum dot (emission wavelength = 800 nm) through immuno-staining using primary antibody (eBioscience, Cat#: 14-4502-80) and secondary antibody conjugated QD800 (ThermoFinsher Scientific. Ref#: Q11071MP). 2000 frames (30ms exposure time) were processed to get SOFI cumulants up to 7th order using both auto- and cross-correlations. In order to better illustrate the origin of cusp artifact, deconvolution and Fourier re-weighting were not included. Among the three pictures for each panel, left picture shows a bigger field of view, where the boxed region is shown in the middle picture, and right picture shows the image where the positive/negative domains are color coded separately. Gamma display is used in this figure, let C_n be the nth order SOFI cumulant, we display here either $|C_n|^{1/n}$ (left/middle pictures) or $s \cdot |C_n|^{1/n}$ (right picture), where s is the $\pm$ sign of each pixel value in C_n. We can see that cusps exist in cumulant with order > 2, the spatial distribution of cusps also differ between different cumulant orders, and they are located at the region with a transition between positive and negative domains. Scale bars: 3.2 μm (left) and 1.6 μm (middle/right) for every panel.

40

In order to better demonstrate the cusp-artifact, we performed a simulation of 3 different blinking emitters with the same on-state brightness, but with on-time ratio equal to 83.1%, 41.6% and 10.3% respectively (Figure 3.2). We can see that the high order cumulants of these three emitters can have either positive or negative peak values at different orders, as predicted from Figure 3.1(v) and listed in Figure 3.2, and cusp-artifacts exist at the region in the image where there is a positive/negative transition of pixel values. In addition, we identified from a real dataset, that we take a gamma display of SOFI cumulants of different orders without taking deconvolution or Fourier re-weighting, as is shown in Figure 3, we can clearly see the cusp artifacts from the SOFI cumulants with order > 2, these cusps are located at the transition region between the positive and negative domains in the image.

3.2.   Conditions that yield cusp-artifact

In order to better understand the significance and effect of cusp-artifact for SOFI reconstruction, we performed a series of simulations. Poisson blinking statistics was used in the simulation, with Gibson Lanni's PSF model. Poisson noise was simulated, and empty frames recorded from EMCCD camera were used to simulate background noise in the conditions where there is background noise. SOFI cumulants up to 7th order are calculated and analyzed.

In the first set of simulation (simulation 3-1), we have three different types of emitters as illustrated in Figure 3.4(i). Assume sufficient statistical significance, we have:

$$\rho = \frac{\tau_{on}}{\tau_{on} + \tau_{off}} \tag{3.3}$$

The estimation of ρ (based on equation (3.2)) of the three populations (P1, P2 and P3) of emitters in the simulation dataset are in the ranges of 0.50 ± 0.1, 0.70 ± 0.17 and 0.52 ± 0.41 respectively,

as shown in Figure 3.4(i) and Figure 3.4(iii). Based on the range of ρ we could predict the signs of virtual brightness of virtual emitters in different cumulant order for each simulated populations, as shown in Figure 3.4(ii). For P1, ρ is distributed in a region with positive lobes of 2nd and 6th order cumulants, negative lobe of 4th order cumulant, and positive/negative transition region of 3rd, 5th and 7th order cumulants. This means all the virtual emitters will exhibit positive virtual brightness in 2nd and 6th order cumulants, negative virtual brightness in the 4th order cumulant, and exhibit both negative and positive virtual brightness in the 3rd, 5th and 7th order cumulants. Based on this information we could predict that P1 can yield cusp-artifact for 3rd, 5th and 7th order of cumulants. Similarly, for P2, ρ is distributed in a region with positive lobes of 2nd and 5th order cumulants, negative lobes of 3rd, 4th and 7th order cumulant, and positive/negative transition region of 6th order cumulants. So we expect Cusp-artifact in cumulants of order 6 for P2. In addition, for P3, ρ is distributed at positive/negative transition region for all the cumulants with order higher than 2, and stay positive for 2nd order cumulant, so P3 can yield cusp-artifact for all cumulants with orders higher than 2. This prediction is clearly shown in Figure 3.4(iii), where 20000 frames of simulation-1 are SOFI processed to ensure sufficient statistical significance of the blinking behavior.

As we reduce the total number of frames to be SOFI processed from simulation 3-1, we start to lose statistical significance of the predicted ρ as well as the independence of blinking trajectories between different emitters, thus we will get unexpected cusp-artifacts in certain cumulant orders, although by prediction from the ground truth τ_{on} and τ_{off} values they supposed to be cusp-artifact free. It is shown that the higher the SOFI order, the more frames are needed for SOFI processing to reach the theoretical prediction of cusp-artifact-free images. But for some of the orders where

the prediction of virtual brightness is a mixture of positive and negative values, the prediction is intrinsically not cusp-artifact free, depends on the order and the actual photo-physical properties of the emitters in the sample.

In the next simulation (simulation 3-2) we imposed bleaching effect to the simulated emitters in simulation 3-1 by stochastically turning the emitters into bleached-state, where they stay at off state till the end of the simulated movie, as illustrated in Figure 3.5(i), Figure 3.5(ii) and Figure 3.5(iii). The overall population of emitters at unbleached status is controlled over time to maintain the pre-calculated bleaching curve (Figure 3.5(i)). We SOFI-processed 20000 frames of the simulation data and have shown that cusp-artifacts exist in cumulants higher than 2nd order. This is because the bleaching of a given individual emitter will intrinsically change the ρ of this emitter over the entire acquired movie and cause its ρ to deviate from the estimation from equation (3.2). Bleaching effect on a group of emitters will thus broaden the apparent distribution of ρ of emitters in the testing sample, as a result, the apparent ρ distribution will expand over a positive/negative transition region as shown in Figure 3.4(i), thus yield a mixture of positive and negative virtual brightness as well as cusp-artifact. In addition, the assumption of independent blinking statistics between different emitters will fail because of the equivalence of long off-state after the emitter is bleached, this further drive the virtual brightness distribution to deviate from the prediction. We then added bleaching correction[3.3] to the simulated data by dividing the whole movie into individual blocks of frames, where each block has signal decrease by $f_{bc} = 1\%$ of the overall signal decrease within the field of view (where f_{bc} is the bleaching correction factor). The final cumulant reconstruction is achieved by averaging all the cumulants calculated from all the individual blocks. After bleaching correction, the prediction of virtual brightness distribution can

be recovered as if there were no bleaching, as shown in Figure 3.5(iv). In addition, in Figure 3.5(iv) when we added recorded empty frames from EMCCD camera to simulate background noise, we find out that the cumulants that intrinsically has both positive/negative virtual brightness are more vulnerable to the background noise, this is because w_n has smaller amplitude around the negative/positive transition region thus attenuates the virtual brightness of virtual emitters in the SOFI cumulants.

Here we want to point out the trade-offs between bleaching correction factor f_{bc}, noise level and statistical significance. When we decrease the bleaching correction factor, the block size will decrease, and the total number of bleaching events happened within each block will decrease, so the bleaching effect is better suppressed, however the signal level per block will decrease thus the reconstruction will be more vulnerable to noise. In addition, statistical significance within each block is decreasing as the block size decreases, we get increased number of blocks for the final construction, so the final cumulant construction in terms of statistical significance is not going to change greatly. If we increase the f_{bc}, we increased the block size thus within each block we get better statistical significance, while more bleaching effect will remain within each block. In summary: Bleaching effect can affect the prediction of cusp-artifact but bleaching correction can diminish this effect. Too small of a f_{bc} will make the SOFI image more vulnerable to background noise. SOFI cumulants that intrinsically have cusp artifacts are more vulnerable to the noise because of the attenuated virtual brightness by small amplitudes of cumulant w_n.
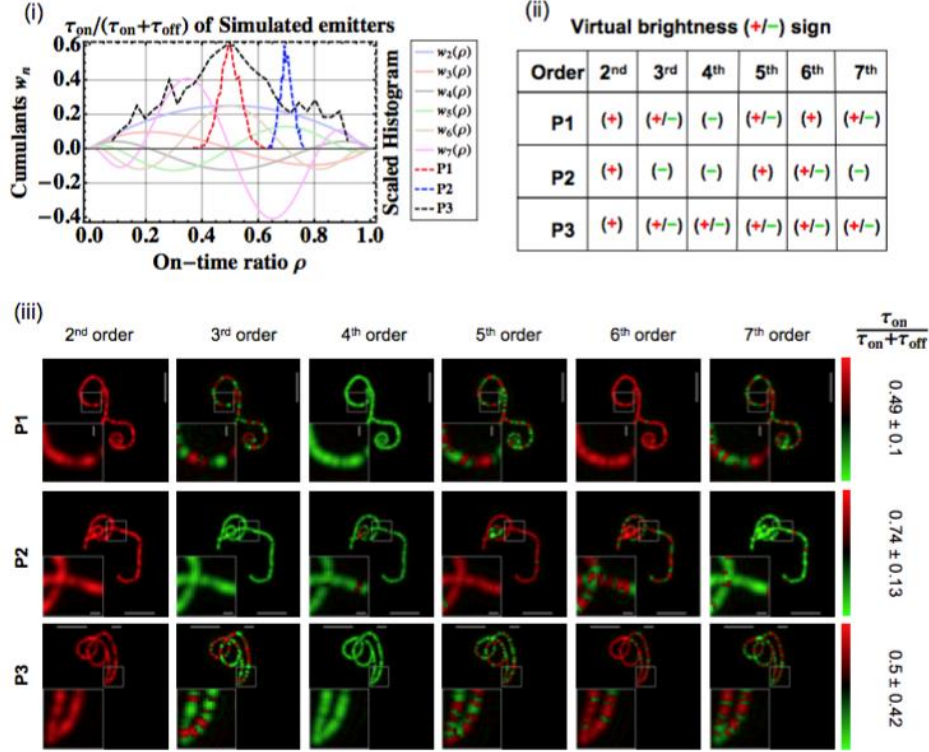
Figure 3.4. Simulation 3-1: Blinking statistics dependence of cusp-artifact.

In this set of simulations, we used 3 different population of simulated emitters that has different distribution of τ_{on} and τ_{off} values, thus yield different distribution of ρ, as illustrated in (i). The predicted virtual brightness signs of P1, P2 and P3 with respect to different cumulant orders are listed in (ii). SOFI processed simulated data is shown in (iii). We can clearly see that the virtual brightness of virtual emitters under different SOFI cumulant orders follows the prediction in (ii), except for certain regions where the simulated feature goes out-of-focus (P2).

In the next simulation (simulation 3-3) we want to see how would cusp artifacts behave if we have spatially slow-varying blinking statistics of emitters in the feature of interest. We prepare a simulated filament with the same type of simulation as we used for simulation-1, but with slow varying input spatial distribution of τ_{on} and τ_{off} (Figure 3.6). SOFI cumulants of 2nd to 7th orders

are calculated, we can see that at a given cumulant order, when the ρ of the emitters reach the transition point of cumulant value we expect a cusp.

3.3. Effect of cusp-artifact on post-processing steps of SOFI

If not handled properly, cusp-artifact can affect the post-processing steps of SOFI, including the direct image display, deconvolution processing, and the balanced cumulant reconstruction in bSOFI. Fourier re-weighting is not affected by cusp-artifact in principal, but cusp-artifact will still present in the Fourier re-weighting result because the virtual brightness will not be changed, thus further post-processing steps like the display of the output and balanced cumulant with still be affected.

When we take the image display by mapping pixel intensity with the amplitude of each pixel value, the cusp-artifact is directly displayed. Because at high order SOFI cumulant reconstruction, the cusp-artifact co-exist with the expanded pixel brightness dynamic range, so it was never clearly identified and discussed in press as an independent factor that degrades the image output perceptibility. In addition, cusp-artifacts can affect the deconvolution step that was proposed to serve as a follow-up post-processing step after high order SOFI cumulants reconstruction. For example, in the MATLAB built-in function deconvlucy and deconvblind, the algorithm has constraints on all the pixel values that force them to be positive values. In practice after each step of iteration, the algorithm automatically set all the negative values to be zero or to be its absolute value. This positive pixel value constraint requires all the ground truth signal source (the true signal to be recovered through deconvolution) to have positive values, thus it conflicts with the cumulant reconstruction when the virtual brightness of the virtual emitters can be negative values. In other words, given a blur image that is in the form of convolution between a ground truth signal that has

a mixture of positive and negative values, and a Gaussian convolution kernel (virtual PSF in this case), the absolute value of this image, it is no longer a proper deconvolution problem thus deconvolution cannot be applied to the image after taking the absolute value of each pixel.
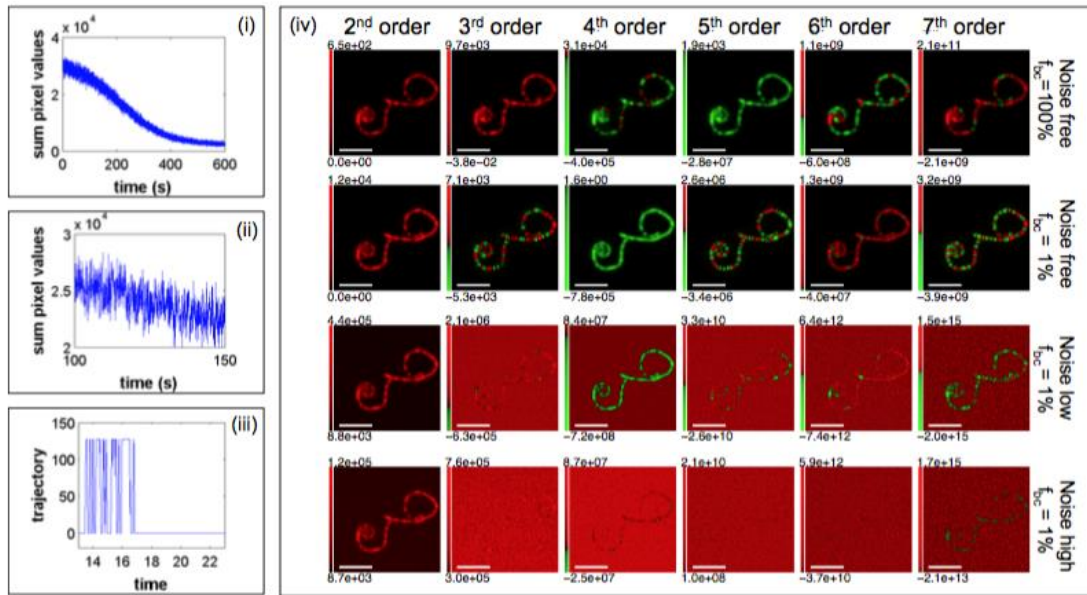
Figure 3.5. Simulation 3-2: Bleaching effect.

This set of simulations shows how cusp artifact behave under bleaching and noisy condition. (i) is the plot of the change of total pixel value over time of our simulated movie before adding the background noise. It shows bleaching curve profile. (ii) is a zoom-in region of (i) where we can still see the fluctuations. (iii) shows an example blinking trajectory of a single emitter, where it was bleached around time 17s, the emitter remains at off state till the end of the movie after it is bleached. (iv) gives the SOFI cumulants display. We can see that bleaching effect changes the virtual brightness prediction ($f_{bc} = 100\%$ means no bleaching correction), but bleaching correction is effective to restore the virtual brightness distribution to the values as if there were no bleaching effect. In addition, for the cumulant orders where we have virtual brightness with mixed +/- signs, the cumulants is heavier affected compared to those orders where the virtual brightness have pure

48

+ or - signs, this is because when the ρ value is distributed around the region to yield (+/-) virtual brightness, $\omega_n(\rho)$ is located at a transition region so the amplitude is brought down because of the small amplitude of $\omega_n(\rho)$ at the transition region. Here we want to point out that the background noise is directly recorded from EMCCD camera as empty frames, and cumulant of background noise is always positive. So negative contrast is possible if we can have a emitter blinking statistics to yield pure negative virtual brightness, as shown here in 4th order cumulant.
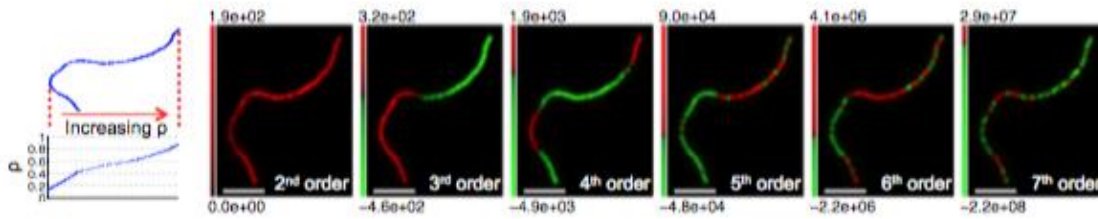

Figure 3.6. Simulation 3-3: Spatially slow varying photo-physics.

In this simulation we put emitters along the feature of interest to have spatial varying ρ, and we can clearly see the cusps at the transition region of positive/negative virtual brightness.

3.4. Cusp-artifact reduction with in-painting

Because cusp-artifact is originated from the intrinsic properties of high order cumulants, on the long term prospective of view, one could seek for methods to avoid cusp-artifacts by tuning the photo-physics properties of the emitters chemically/physically in order to achieve a pure positive or negative virtual brightness for a certain order of SOFI cumulant. As a compromise, we here by present one method to fill-in the cusps using in-painting algorithm [3.2]. As illustrated in Figure 3.7, for high order SOFI cumulant image we will have positive domains and negative domains and cusps are located at the transition area of positive/negative domains. In order to apply in-painting to the cusps, first we identify the cusp region by detecting the positive/negative domain transition region, then we extend the width of the region by a given radius (empirically we use 5 pixels wide, but this width is dependent on the pixel size and the virtual PSF size.) to get the area to be inpainted (region m). The goal is to refill the identified region using the surrounding information from the image. Our implementation extends the isophotes of the image from surrounding the region m into region m thus yield a smooth inpaint of pixel values within the region identified, so the gaps created by the cusps will thus be smoothed. The algorithm is implemented according to the method developed by Bertalmio, et al [3.2]. with minor modifications. In addition, a local image dynamic range compression method (dubbed as "ldrc" method) were developed to correct for the image dynamic range expansion problem (details to be discussed in Chapter 5) of high order SOFI. We compared the in-painting and ldrc enhanced 6th order SOFI cumulants reconstruction with bSOFI, using both simulation and experimental data, and have shown that under many circumstances it can give us faithful representations.
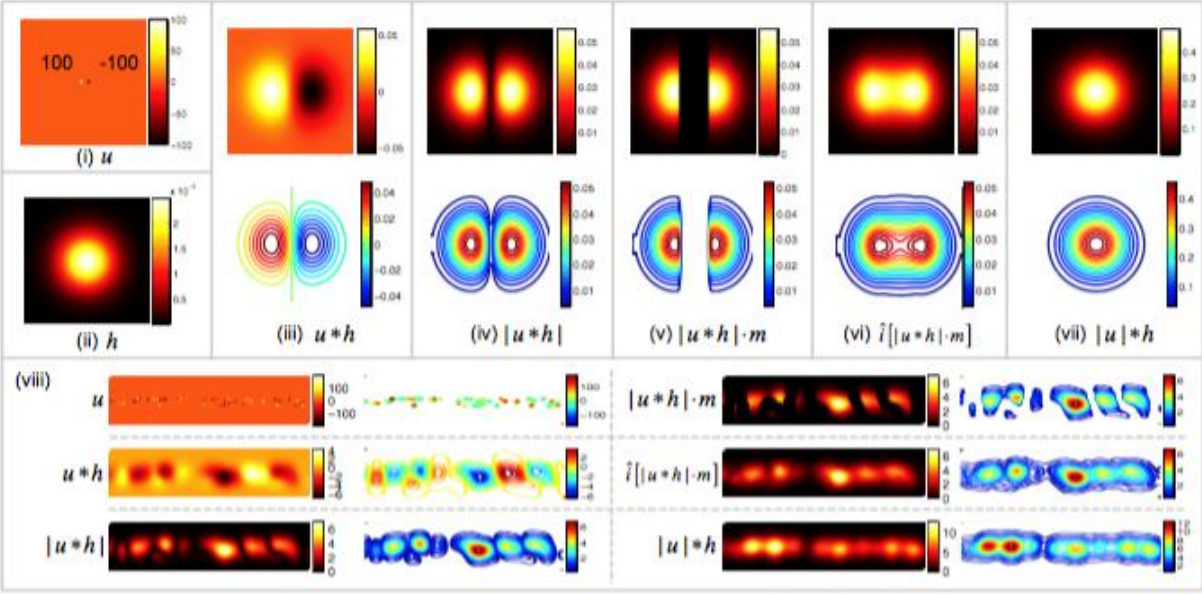
Figure 3.7. Cusp-artifact reduction with inpainting.

Suppose we start with two virtual emitters with positive and negative virtual brightness (with the ground truth image denoted as u) as shown in (i), and suppose the current virtual PSF (denote as h) is demonstrated in (ii), the cumulant will thus be the convolution between u and h, as shown in (iii). Take the absolute value of $u*h$ (where $*$ represents convolution operation) we get a cusp artifact at the positive/negative domain transition region as shown in (iv). We use m to represent for the identified region to be inpainted, where we have $m(i, j) = 0$ if pixel at location (i, j) is within the identified region to be inpainted, and $m(i, j) = 1$ otherwise. $(\cdot)$ represent for entry-wise multiplication. The inpainting result is shown in (vi) where $\hat{i}$ stand for inpainting operation. We can see the smooth connection between the sides of the gap. (vii) shows the equivalence of a blur image if we force all the virtual brightness to be positive value. We want to point out that inpainting enhanced high order cumulant is not feasible for balanced cumulant reconstruction in bSOFI, as we can tell from the difference between (vi) and (vii). Another simulation is with more virtual

51

emitters located alone a line is shown in (viii), we can see here that inpainting result indeed shows faithful reconstruction.

3.5.   Effect of cusp-artifact on high order moments reconstruction

In addition, because of the valuable fact that even-order moments are intrinsically cusp-artifact free, we analyzed the cusp artifacts on moments reconstruction from all the cumulants reconstructed from cross-correlations. Moments was initially rejected due to the mixed terms that contain signal contributed from multiple individual emitters, rendering the physical meaning of the resulting image hard to interpret. We here-by tested the moments reconstruction and find out that moments indeed pro- vides enhanced resolution from simulations by comparing to the ground truth as well as from cross-section plots, as shown in Figure 3.8. A full understanding of moments reconstruction at high orders is yet to be investigated in the future.
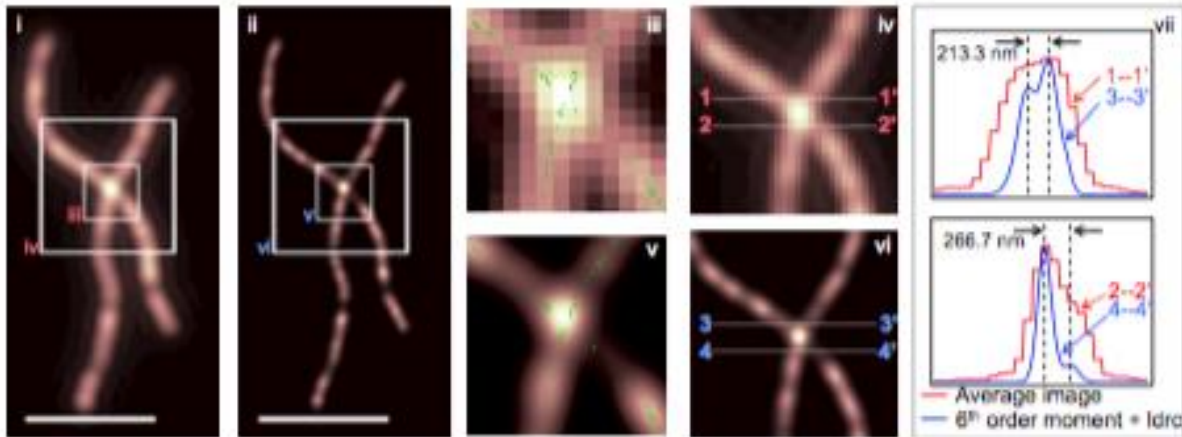
Figure 3.8. Simulation 3-5, 6th order moments.

(i) shows the sum image of this simulation (ii) shows the 6th order moment reconstruction combined with local dynamic range compression. Boxed region in both (i) and (ii) are shown in (iii), (iv), (v) and (vi) as labeled in the figure. In panel (iii) and (v), green dots mark the exact locations of emitters in the simulation, and we can see that the 6th order moment indeed shown some faithful information as compared to the ground truth of the location of emitters. Two cross sections labeled in (iv) and (vi) are plotted in (vii).

3.6. Performance comparisons on real data

In this section we tested and compared inpainting enhanced 6th order SOFI cumulant, 6th order moment reconstruction as well as bSOFI on experimental data. We labeled the α-tubulin on fixed Hela cells using QD800. As shown in Figure 3.9(i), (ii), (iii), (iv) show the large field of view of the average image, 2nd order SOFI cumulant with extra pixels from cross-correlations (XC2), Local dynamic range compressed (ldrc) 6th order moment (M6) reconstructed from cumulants with extra pixels provided from cross-correlations (M6+ldrc), and balanced cumulant reconstruction using 2nd, 3rd and 4th order cumulants (bSOFI), respectively. No deconvolution or Fourier reweighting is involved in XC2 or M6 in order to isolate the factors of resolution enhancement, bSOFI involves deconvolution because balanced cumulant reconstruction is a post-processing step after deconvolution. We can see that both XC2 and M6+ldrc shows faithful image reconstruction, at the region where the feature density is low and α-tubulins are well separated, XC2 and bSOFI performs better than M6+ldrc in terms of feature visibility. How- ever, at the image region where the feature of interest is dense, as shown in the boxed region in Figure 3.9(i) and displayed in Figure 3.9(v), (vii), (viii) and (iv) respectively, we can see that M6-ldrc starts to out-perform XC2 and bSOFI. In the case of inpainting enhanced cumulant, we performed local dynamic range compression on 6th order SOFI cumulant with extra pixels provided by cross- correlations as shown in Figure 3.9(x), and detected the region where there is a transition between positive domain and negative domain in the image and broaden the region to be the region to be inpainted, as shown in Figure 3.9(xi), and the inpainting result is shown in Figure 3.9(xii).
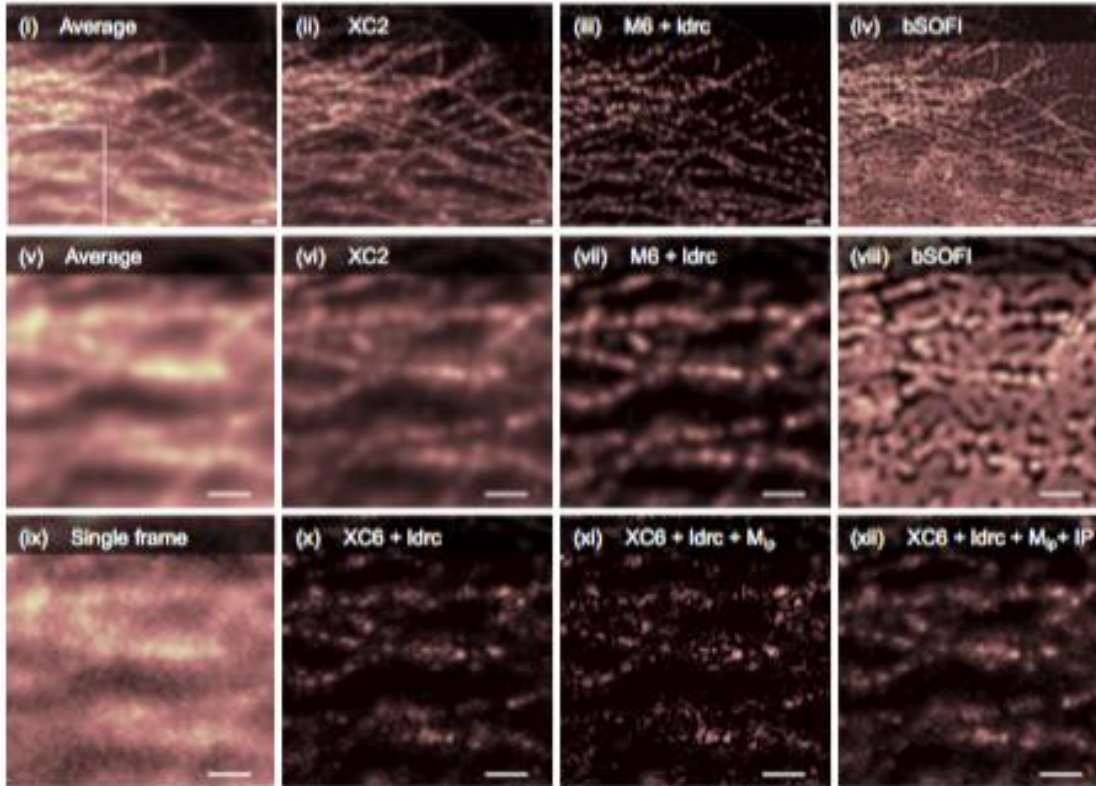
Figure 3.9. QD800 labeled α-tubulin of fixed Hela cell.

Panel (i), (ii), (iii), (iv) are larger field of view of the data set. The rest of the panels shows the zoom-in images that corresponds to the area shown in the boxed region in (i). We take 2000 frames with 30ms in this dataset, (i) and (v) show the average signal from the dataset, (ix) is an example single frame of the dataset. (ii) and (vi) shows the 2nd order SOFI cumulant with extra pixels from cross-correlations (XC2). (iii) and (vii) shows the 6th order moment (M6) reconstructed from cumulants, with local dynamic range compression (ldrc). (iv) and (viii) shows bSOFI of balanced cumulant reconstruction from cumulants with all the lower orders. (x) is the 6th order cumulant with extra pixels from cross-correlations(XC6), combined with local dynamic range compression (ldrc). (xi) is the XC6+ldrc with the pixel values located within the inpainting mask set to 0, and (xii) is the inpainting result of XC6. Scale bars: 1.6μm

56

3.7.   Discussions

In general, 2nd order cumulants is not jeopardized by cusp-artifacts because virtual emitters of 2nd order cumulants in principal cannot yield negative virtual brightness. For cumulants with order > 2, the significance of cusp-artifact can be summarized as follows: First, if the number of frames SOFI-processed is not large enough to exhibit statistical significance of blinking behavior, cusp-artifact is expected for cumulants higher than 2nd order. This is shown in simulation-1. Cusp-artifact exist in cumulants with order > 2 if 2000 frames are SOFI-processed, but has the chance to be avoided if more frames are SOFI-processed to ensure statistical significance, but this is not guaranteed for every circumstance. Second, given that there is statistical significance of blinking behavior in the imaging sample, a fixed expectation value of ρ for given blinking statistics is required to avoid cusp-artifact. This is because if the blinking statistics doesn't ensure fixed expectation value of ρ for the emitters in the testing sample, the apparent ρ could have a wide range of values that yield co-existence of positive/negative virtual brightness in a given order of cumulants. Third, given statistical significance and fixed expectation value of ρ, if the range of ρ covers a transition region on a given order of cumulant, cusp-artifact is expected at the order of cumulant. No matter if the photo-physical properties is spatially slow varying or fast varying.

Fourth, given statistical significance, fixed expectation value of ρ and desired range of ρ without positive/negative transition for a give order of cumulant, bleaching effect can still impose a cusp-artifact to the image reconstruction. In summary, in order to avoid cusp-artifact, one would consider four conditions: 1), choose the labeling emitters that has intrinsic expectation value of ρ, 2), acquire dataset that is long enough to hold statistical significance of blinking behavior of all

the emitters in the imaging sample, 3) manage to have a desired range of ρ distribution that does not cover a positive/negative transition region for the chosen order of cumulants, 4) avoid bleaching or perform bleaching correction to the dataset, given that in the bleaching correction approach, condition-1 to -3 should be fulfilled within each bleaching correction block. In addition, given a SOFI cumulant that already has cusp artifact, we can use inpainting algorithms to fill-in the gaps created by the cusps, or avoid the cusp-artifacts by using moments reconstruction.

3.8. References

[3.1].   M. G. Kendal. 1946. The advanced theory of statistics.

[3.2]. M. Bertalmio, G. Sapiro, et al.2000. Image inpainting. Proceedings of the 27th annual conference on Computer graphics and interactive techniques.

[3.3]. Dertinger, Thomas, et al. "Achieving increased resolution and more pixels with Superresolution Optical Fluctuation Imaging (SOFI)." *Optics express* 18.18 (2010): 18875-18885.

Chapter 4. Moments reconstruction of high order SOFI

In order to avoid cusp artifacts created by the negative/positive brightness of virtual emitters in the high order SOFI cumulant image, we evaluated the moments reconstruction and have empirically shown that moments can give a faithful reconstruction at high orders. In this chapter, we will first introduce the algorithm for moments reconstruction, followed by theoretical evaluation of high order moments reconstruction. In the end, we will demonstrate the performance of moments reconstruction on real data.

4.1.   Algorithm for moments reconstruction

The algorithm for moments reconstruction is based on the interchangeable relationship between cumulants and moments[4.1], and is illustrated in Figure 4.1. First the fluctuation of the fluorescence signal is calculated at each original pixel. Then SOFI cumulant at different order is calculated with cross-correlation from different pixels to yield virtual pixels. Then Fourier back projection is performed on every order of SOFI cumulant to match the grid of the image matrixes so at one location there exist cumulant of different orders. Then using the interchangeable relationship between cumulant and moments below:

$$M_n(\vec{r};\tau=0) = \sum_{\substack{\text{all partitions of} \\ I_1 \cup I_2 \cup \cdots \cup I_p \\ =\{1,2,\dots,n\}}} C_{s_1}(\vec{r},\tau=0)\cdots C_{s_p}(\vec{r},\tau=0)$$

(4.1)

where s_p is the total number of element in part I_p

We can perform moments reconstruction as above.
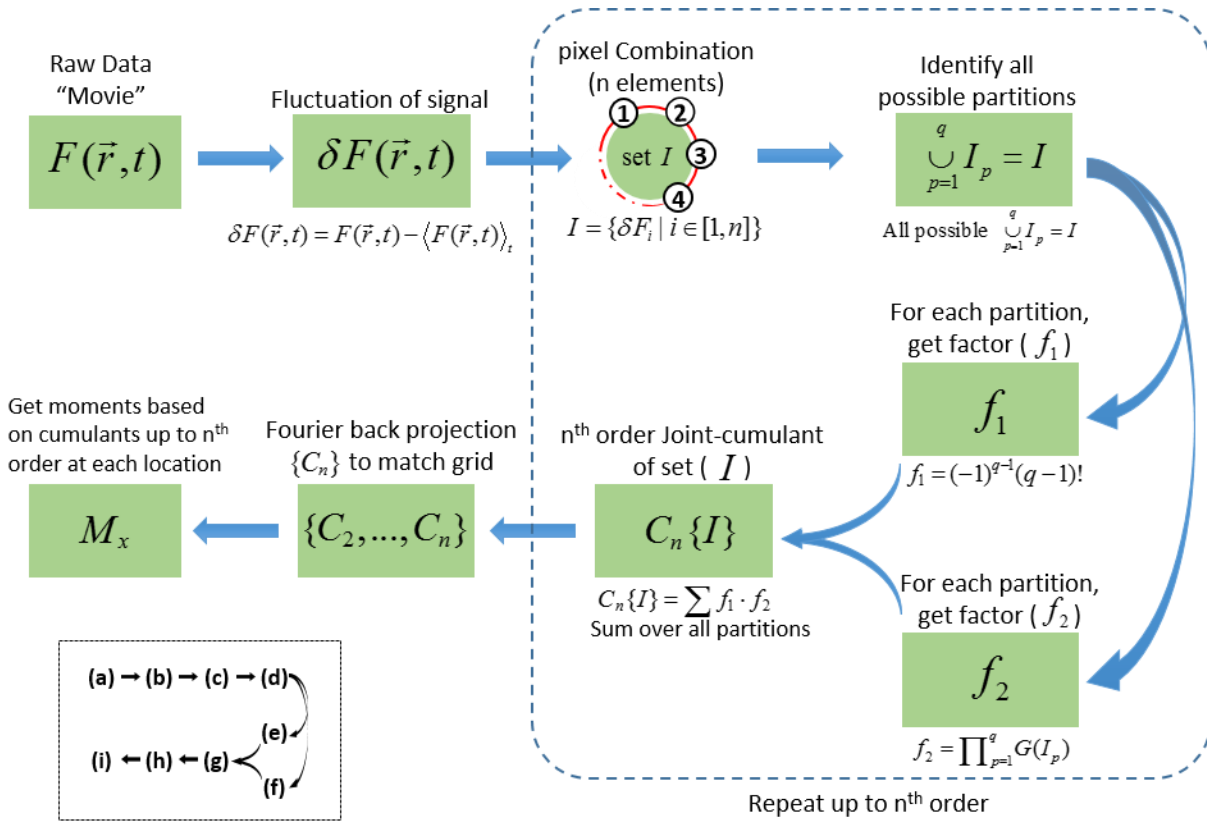
Figure 4.1. Algorithm of moments reconstruction for high order SOFI.

Step (a) to step (g) shows the conventional way of SOFI cumulant calculation with cross-correlations and extra pixels. Step (h) will match the image matrix onto the same grids using interpolation algorithm. In practice Fourier transform back projection is used to match the matrix grid for different order of cumulants, such that at each location there is a full set of cumulant values from 2nd order to n^{th} order, to perform the moments reconstruction.

4.2. Theoretical evaluation of high order moments

Because we have

$$C_n(\vec{r}) = \sum_{k=1}^{N} \epsilon_k^n C_n(\delta b_k(t)) U^n(\vec{r} - \vec{r}_k) \tag{4.2}$$

For a given set of n elements, if we have one partition of set $\{1,2,3,...,n\}$ as $\{I_p \mid p = 1,2,...,\sigma\}$, so

we have $I_1 \cup I_2 \cup \cdots \cup I_\sigma = \{1,2,3,...,n\}$, and if we denote s_p as the total number of element in part

I_p, we have:

$$\sum_{p=1}^{\sigma} S_p = n \tag{4.3}$$

Substitute equation (4.2) into equation (4.1) and focus on the expression inside the summation

series, we have:

$$C_{s_1}(\vec{r}) \cdots C_{s_\sigma}(\vec{r}) = \left(\sum_{k=1}^{N} \epsilon_k^{s_1} C_{s_1}(\delta b_k(t)) U^{s_1}(\vec{r} - \vec{r}_k) \right) \cdots \left(\sum_{k=1}^{N} \epsilon_k^{s_\sigma} C_{s_\sigma}(\delta b_k(t)) U^{s_\sigma}(\vec{r} - \vec{r}_k) \right)$$
$$= \sum_{k_1=1}^{N} \cdots \sum_{k_\sigma=1}^{N} \left(\prod_{p=1}^{\sigma} \epsilon_{k_p}^{s_p} \right) \left(\prod_{p=1}^{\sigma} C_{s_p}(\delta b_{k_p}(t)) \right) \left(\prod_{p=1}^{\sigma} U^{s_p}(\vec{r} - \vec{r}_{k_p}) \right) \tag{4.4}$$

Because we have:

$$\prod_{p=1}^{\sigma} U^{s_p}(\vec{r} - \vec{r}_{k_p}) = U^n(\vec{r} - \frac{1}{n}\sum_{p=1}^{\sigma} S_p \cdot \vec{r}_{k_p}) W(\{s_p, \vec{r}_{k_p} \mid p \in [1,\sigma]\}) \tag{4.5}$$

So equation (4.4) becomes:

$$C_{s_1}(\vec{r}) \cdots C_{s_\sigma}(\vec{r})$$
$$= \sum_{k_1=1}^{N} \cdots \sum_{k_\sigma=1}^{N} \left(\prod_{p=1}^{\sigma} \epsilon_{k_p}^{s_p}(\vec{r}) \right) \left(\prod_{p=1}^{\sigma} C_{s_p}(\delta b_{k_p}(\vec{r})) \right) \left(U^n(\vec{r} - \frac{1}{n}\sum_{p=1}^{\sigma} S_p \cdot \vec{r}_{k_p}) W(\{s_p, \vec{r}_{k_p} \mid p \in [1,\sigma]\}) \right) \tag{4.6}$$

We can re-write the summation above ($\sum_{k_1=1}^{N} \cdots \sum_{k_\sigma=1}^{N} (\cdot)$) into summation over all possible combinations

of $\{k_p \mid p \in [1,\sigma]\}$ with $k_p \in [1,N]$. Introduce two extra simplification of notations as

$$\frac{1}{n}\sum_{p=1}^{\sigma} S_p \cdot \vec{r}_{k_p} = \vec{r}_g\left(\{S_p, k_p\}\right) = \vec{r}_k \tag{4.7}$$

and

$$W(\{S_p, \vec{r}_{k_p} \mid p \in [1,\sigma]\}) = W(\{S_p, \vec{r}_{k_p}\}) \tag{4.8}$$

equation (4.6) becomes:

$$C_{s_1}(\vec{r})\cdots C_{s_\sigma}(\vec{r}) = \sum_{\{k_p \mid p \in [1,\sigma]\}}^{k_p \in [1,N]} \prod_{p=1}^{\sigma} \epsilon_{k_p}^{S_p}(\vec{r}) \left(\prod_{p=1}^{\sigma} C_{s_p}(\delta b_{k_p}(\vec{r}))\right)\left(U^n(\vec{r} - \vec{r}_g(\{S_p, \vec{r}_{k_p}\}))W(\{s_p, \vec{r}_{k_p}\})\right)$$

$$(4.9)$$

Substitute into equation (4.1), we get:

$$M_n(\vec{r}; \tau = 0) = \sum_{\substack{\text{all partitions of} \\ I_1 \cup I_2 \cup \cdots \cup I_p \\ =\{1,2,\ldots,n\}}} C_{s_1}(\vec{r}, \tau = 0) \cdots C_{s_p}(\vec{r}, \tau = 0)$$

$$= \sum_{\substack{\text{all partitions of} \\ I_1 \cup I_2 \cup \cdots \cup I_p \\ =\{1,2,\ldots,n\}}} \sum_{\{k_p \mid p \in [1,\sigma]\}}^{k_p \in [1,N]} \left(\prod_{p=1}^{\sigma} \epsilon_{k_p}^{S_p}(\vec{r})\right)\left(\prod_{p=1}^{\sigma} C_{s_p}(\delta b_{k_p}(\vec{r}))\right)\left(U^n\left(\vec{r} - \vec{r}_g\left(\{S_p, \vec{r}_{k_p}\}\right)\right)W\left(\{s_p, \vec{r}_{k_p}\}\right)\right)$$

$$(4.10)$$

When the coordinates $\{k_p \mid p \in [1,\sigma]\}$ is identical (denote as $\vec{r}_k$), we have

$W(\{s_p, \vec{r}_{k_p} \mid p \in [1,\sigma]\}) = 1$, and $\frac{1}{n}\sum_{p=1}^{\sigma} S_p \cdot \vec{r}_{k_p} = \vec{r}_g\left(\{S_p, k_p\}\right) = \vec{r}_k$. This means the signal is

equivalence to a virtual emitter that is located at the same location of the original emitter. When

the coordinates of $W(\{s_p \vec{r}_{k_p} \mid p \in [1,\sigma]\})$ is different, we have $W(\{s_p \vec{r}_{k_p} \mid p \in [1,\sigma]\}) < 1$. So that

means within all the terms in the summation series of the signal in equation (4.4), the term that

contains identical coordinates in $\{k_p \mid p \in [1, \sigma]\}$ contains the highest portion. This is the term when we have $k_1 = k_2 = ... = k_\sigma$. If we denote this identical k coordinates as k, the term from equation (4.10) can be expressed as follows:

$$\sum_{\substack{\text{all partitions of } \{k_p \mid p \in [1,\sigma]\} \\ I_1 \cup I_2 \cup \cdots \cup I_p \\ =\{1,2,...,n\}}} \sum_{\substack{k_p \in [1,N] \\ k_1 = \cdots = k_p = k}} \left(\prod_{p=1}^{\sigma} \epsilon_{k_p}^{S_p}(\vec{r}) \right) \left(\prod_{p=1}^{\sigma} C_{s_p}(\delta b(\vec{r})) \right) \left(U^n \left(\vec{r} - \vec{r}_g \left(\{ S_p, \vec{r}_{k_p} \} \right) \right) \right) W \left(\{ s_p, \vec{r}_{k_p} \} \right)$$

$$= \sum_{\substack{\text{all partitions of} \\ I_1 \cup I_2 \cup \cdots \cup I_p \\ =\{1,2,...,n\}}} \sum_{k=1}^{N} \epsilon_k^n(\vec{r}) \left(\prod_{p=1}^{\sigma} C_{s_p}(\delta b_k(\vec{r})) \right) U^n(\vec{r} - \vec{r}_k) \qquad (4.11)$$

$$= \sum_{k=1}^{N} \epsilon_k^n(\vec{r}) U^n(\vec{r} - \vec{r}_k) \sum_{\substack{\text{all partitions of} \\ I_1 \cup I_2 \cup \cdots \cup I_p \\ =\{1,2,...,n\}}} \left(\prod_{p=1}^{\sigma} C_{s_p}(\delta b_k(\vec{r})) \right)$$

Because we have:

$$\sum_{\substack{\text{all partitions of} \\ I_1 \cup I_2 \cup \cdots \cup I_p \\ =\{1,2,...,n\}}} \left(\prod_{p=1}^{\sigma} C_{s_p}(\delta b_k(\vec{r})) \right) = M_n(\delta b_k(\vec{r})) \qquad (4.12)$$

The expression shown in equation (4.11) becomes:

$$\sum_{k=1}^{N} \epsilon_k^n(\vec{r}) U^n(\vec{r} - \vec{r}_k) M_n(\delta b_k(\vec{r})) \qquad (4.13)$$

This term is intrinsically equivalence to a virtual image. Under the virtual emitter interpretation, the image is formed with virtual PSF as the original PSF raised to the power of n, by virtual emitters located at the original emitter location but carries virtual brightness as the product of the original 'on'-stage brightness raised to the power of n and the nth order moment of the fluctuation profile of the emitter. Take this term back into equation (4.10), we have:

$$M_n(\vec{r};\tau=0) = \sum_{k=1}^{N} \epsilon_k^n(\vec{r}) U^n(\vec{r}-\vec{r}_k) M_n(\delta b_k(\vec{r}))$$

$$+ \sum_{\substack{\text{all partitions of} \\ I_1 \cup I_2 \cup \cdots \cup I_p \\ =\{1,2,\ldots,n\}}} \left[\sum_{\substack{\{k_p|p\in[1,\sigma]\} \\ \text{no repeating } k_p}}^{k_p\in[1,N]} \left(\prod_{p=1}^{\sigma} \epsilon_{k_p}^{S_p}(\vec{r}) \right) \left(\prod_{p=1}^{\sigma} C_{s_p}(\delta b_{k_p}(\vec{r})) \right) \left(U^n\left(\vec{r}-\vec{r}_g\left(\{S_p,\vec{r}_{k_p}\}\right)\right) \right) W\left(\{s_p,\vec{r}_{k_p}\}\right) \right]$$

(4.14)

Based on the expression above, we can interpret the moment reconstruction as two different portion of signals. Both portion of the signals can be viewed as with virtual point spread function that is n^{th} power of the original PSF. Be in terms of the signal source, the first portion is signal contributed from virtual emitters that are located at exactly the same locations of the original emitters, but have virtual brightness as the product of two factors, where the first factor is the original 'on'-stage brightness raised to the power of n and the second factor is the nth order moment of the fluctuation of the blinking profile of the corresponding original emitter. The second portion of the signal is much more complicated and a thorough investigation is still difficult. But we can see that this portion of the signal can be interpreted as the emitter located at weighted geometry center described in equation (4.7), and the virtual brightness is not only determined by an equivalence cumulant value and the brightness value, but also attenuated by factor $M_n(\delta b_k(\vec{r}))$. We expect this second portion to serve as extra virtual emitters to fill-in the gaps left by the original emitters.

4.3. Evaluation of moments on simulation and experimental data.

We first evaluate the moments value as a function of 'on'-time ratio ρ as defined in the previous chapter and find out that moments are always positive at even orders. As shown in Figure 421. And also evaluate the value of moments with 3 emitters simulation as shown in Figure 4.2, we show here that the brightness ratio of the peak value of each individual emitter of follows the

theoretical prediction. We also show the performance of moments reconstruction in Figure 4.3 on real data from Quantum dot labeled microtubules. The direct reconstruction of cumulant and moments both suffers from the image brightness dynamic range expansion such that the dim part of the image is hardly perceptible, as shown in panel (a) and (c) in Figure 4.3. So we take the gamma display of the image by showing the pixel intensity as the original pixel intensity raised to the power of $\frac{1}{6}$ as shown in (b) and (c) accordingly. We can see from the zoom in area that for the 6th order cumulant, we have cusp-artifact. However, with 6th order moment reconstruction as shown in (d), we no longer have cusp artifacts.
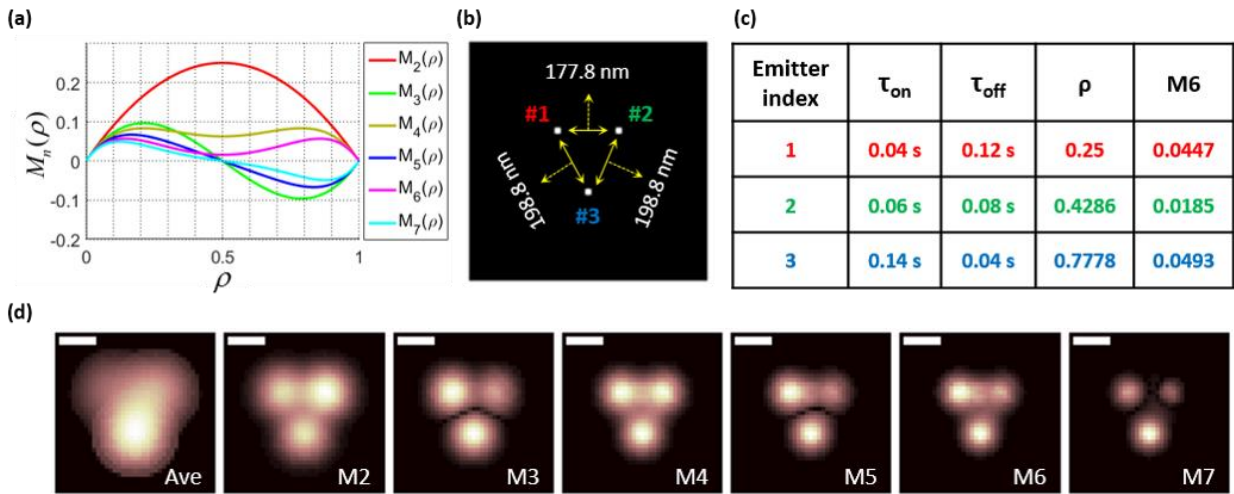
Figure 4.2. Moments evaluation with theory and simulation.

(a) shows the theoretical plot of different order of moments as a function of 'on'-state ratio ρ (

n^{th} order moment is shown as $M_n(\rho)$), and we show here that moments of 2nd, 4th, and 6th order

is always positive. (b) (c) (d) shows the simulation of a 3-emitters that follows Poisson blinking

statistics to verify the values of moments reconstruction. (b) shows the ground truth of the spatial

locations of the 3 emitters, and (c) shows the ground truth blinking statistics of the three emitters.

(d) shows the moments reconstruction of the simulated movie at different orders (labeled as " *Mn*

" with $n \in [2,7]$) as well as the average image (labeled as "Ave"). we can see the moments with

even orders doesn't carry cusp artifact, in addition, the peak value intensity ratio follows the values

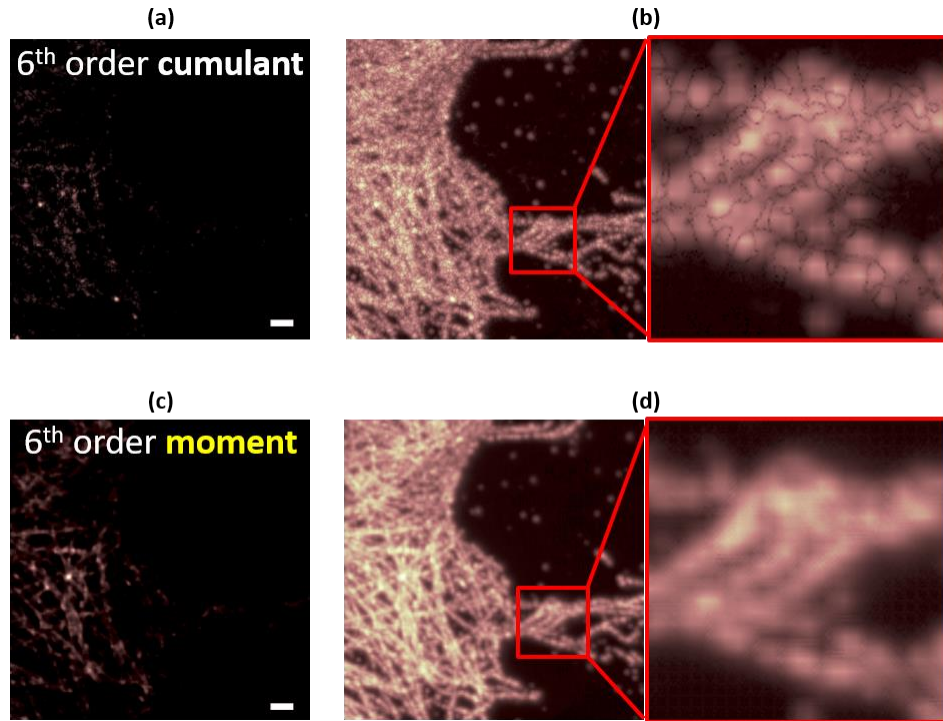predicted from the ground truth blinking statistics as shown in panel (c).

Figure 4.3. Moments reconstruction on real data.

This is fixed 3T3 cells labeled with quantum dot 625, the labeled structure is α-tubulin. (a) shows

the 6th order cumulant displayed at the original scale, and (b) shows the gamma scale display with

$\gamma = \dfrac{1}{6}$. right panel of panel (b) shows the zoom-in region as shown in the left panel in the red box

region. (c) shows the 6th order moment and (d) shows the gamma scale display of (c) accordingly.

We can see here that under moments reconstruction, the image shows no cusp artifacts. Scale bar:

1.6 μm .

4.4.   Reference

M. G. Kendal. 1946. The advanced theory of statistics.

Chapter 5. Local dynamic range compression of high order SOFI

Aside from the cusp artifact, high order SOFI suffers from the nonlinear expansion of pixel intensity dynamic range. Although in the previous chapter we have demonstrated moments reconstruction as a concession to avoid cusp artifact, but the dynamic range expansion problem persists. As can be seen in Figure 5.1, we have shown the moments reconstruction result of different orders. The feature of interest in the image becomes less perceptible as the SOFI order increases. In this chapter, we aim for compression of such dynamic range to reveal the hidden information without introducing too much artifacts, as well as retaining the improved resolution. The algorithm is shown in Figure. 5.2, the first step is to choose a reference image that doesn't carry severe expansion of pixel intensity dynamic range. Empirically we choose the second order SOFI image to be this reference image. The high order SOFI image is rescaled with respect to this reference image, where a small window is defined in the high order SOFI image, and the local dynamic range is rescaled with respect to the area in the same window from the reference image. It is worth noticing here that during the dynamic range rescaling process, we keep the minimal pixel value intact, and linearly stretch the pixel values to have the maximum pixel value in the windowed area to match the maximum pixel value of the window are in the reference image. We perform this local dynamic range compression over the entire field of view to obtain ldrc-SOFI reconstruction.
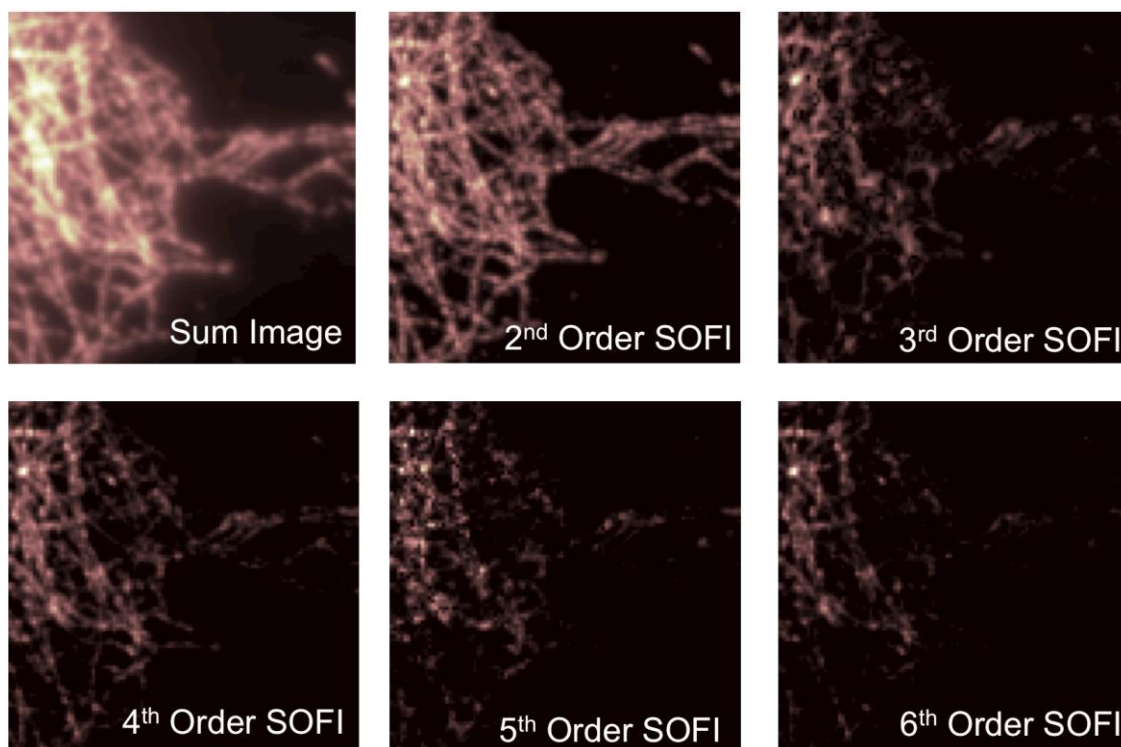
Figure 5.1. Pixel intensity dynamic range expansion.

In this image we demonstrate a fixed 3T3 cell with microtubules labeled with QD625. Moments reconstruction of different SOFI order is demonstrated. It is worth noticing here that for fluctuation sequence that is center-shifted (subtracted the time average), 2nd order cumulant and 2nd order moment are identical. We can see here that as the SOFI order increases, the pixel intensity dynamic range expands such that the details of the feature of interest becomes imperceptible.
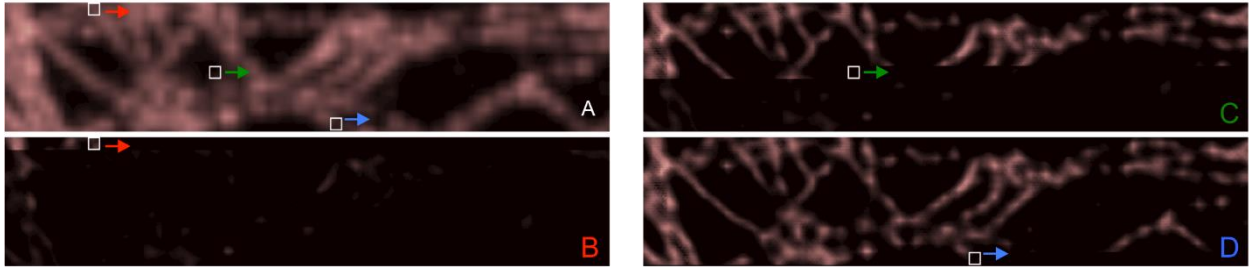
Figure 5.2. Algorithm of Local Dynamic Range Compression (ldrc).

In this example we used second order SOFI as the reference image as shown in panel A. The corresponding field of view of 6th order moment reconstruction is shown in panel B. we define a small window and rescale the pixel intensity inside the window with respect to the pixel intensity scale in the same area from the reference image. We slide the window pixel-wise across the entire field of view and stich all the rescaled windows together to form the final reconstructed image, as shown in panel C and D. Such computation can be performed in parallel because the rescaling of different window regions are independent processes.

The performance of this ldrc-SOFI is demonstrated on fixed 3T3 cells with microtubules labeled with QD625 through immuno-staining, and compared to bSOFI reconstruction, as shown in Figure 5.3. and Figure 5.4.
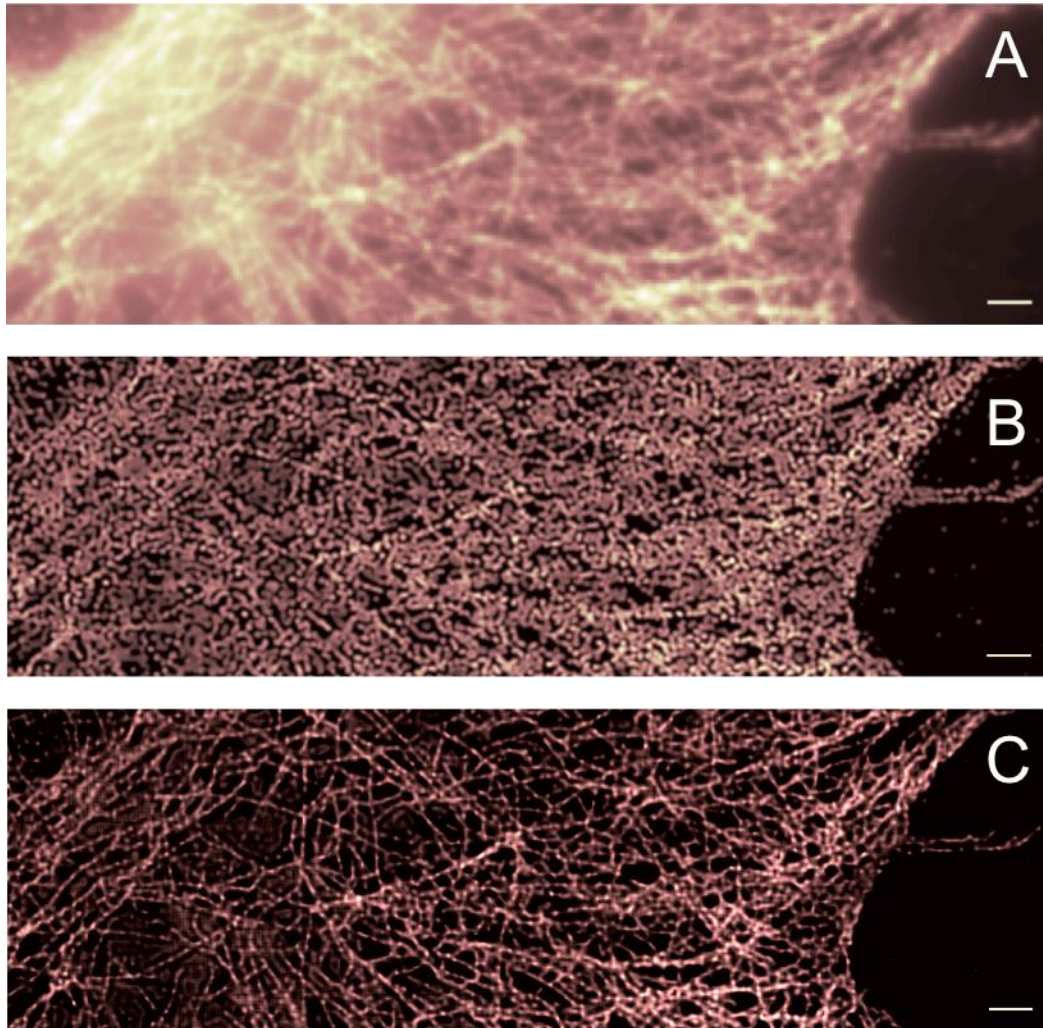
Figure 5.3. Comparison of ldrc-SOFI with bSOFI.

The image shows the performance of ldrc-SOFI and bSOFI on Fixed 3T3 cell with QD625 labeled α-tubulin (A) Time average of the entire movie. (B) bSOFI result. (C) ldrc-SOFI of 6th order moment. Total of 2000 frames were processed for each method. We can see ldrc-SOFI suffers from fewer artifacts, while exhibiting faithful dynamic range compression. Scale bar: 2 um. 2000 frames were processed.

Figure 5.4. Cross-section analysis.

Fixed 3T3 cell with QD625 labeled α-tubulin, cross-section analysis shows ldrc-SOFI holds about

4-fold resolution enhancement

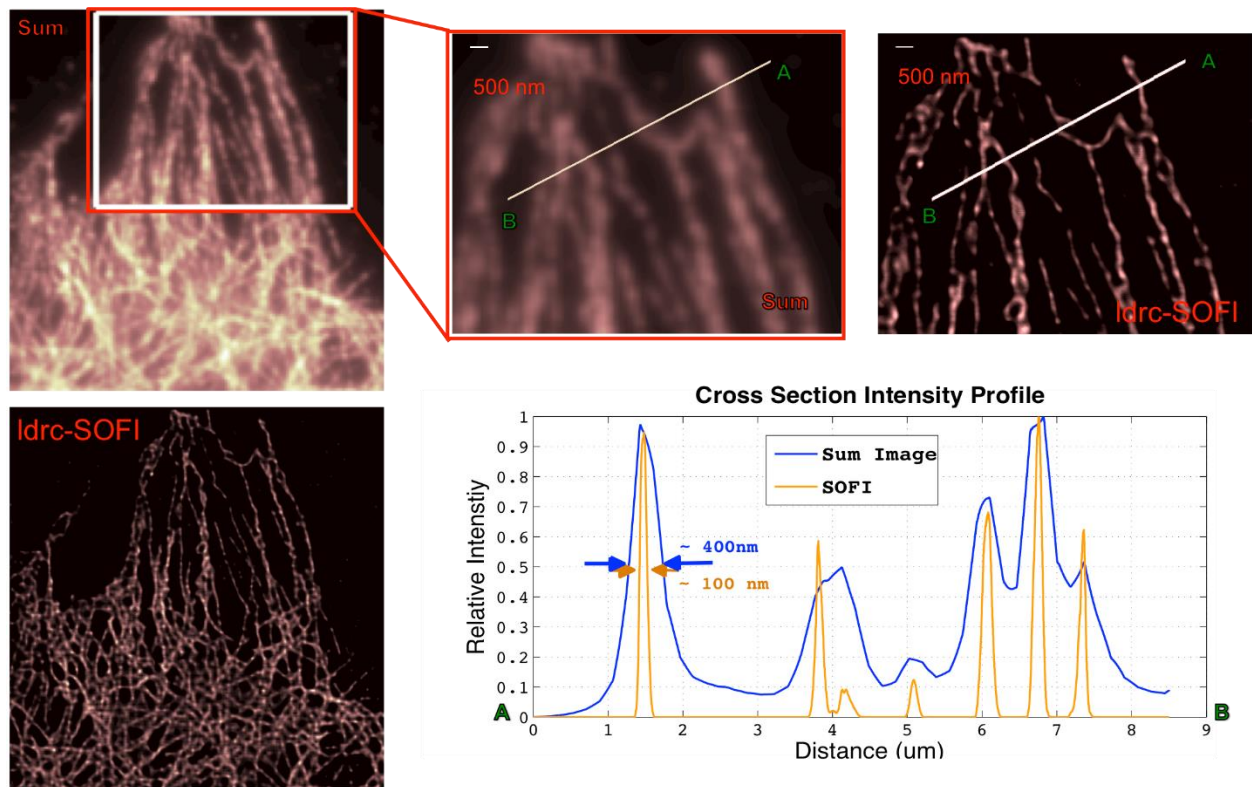A large library of simulated data of filaments networks with variable filaments density, labeling density, labeling uncertainty, noise level, background level and nonspecific binding probability are generated and examined by both bSOFI and ldrc-SOFI. When the signal to noise ratio (SNR) and other sample conditions are favorable, both algorithms perform well. In fact, under very low filaments density bSOFI performs better. However, under challenging imaging conditions (high feature density, non-specific background, high noise level), ldrc-SOFI yields better performance with fewer artifacts, as shown in Figure 5.5 to Figure 5.8.

Figure 5.5. Simulation of filaments with different labeling density.

(a) shows the ground truth for this simulation. Two different labeling densities are simulated in this simulation. In **(b, d, f),** high labeling density condition (105 emitters per 100 nm) are analyzed for the sum image **(b)**, ldrc-SOFI **(d)**, and bSOFI **(f)** respectively. In **(c, e, g)**, low labeling density condition (25 emitters per 100nm) are analyzed for the sum image **(c)**, ldrc-SOFI **(e)**, and bSOFI **(g)** respectively. Scale bar: 2 um.
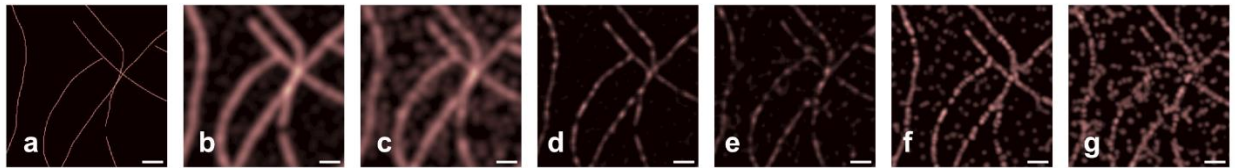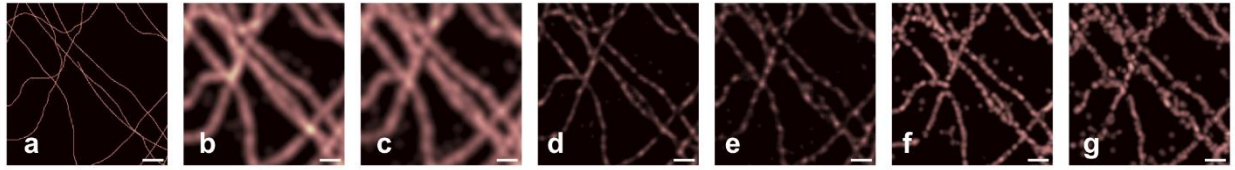
Figure 5.6. Simulation of filaments with different labeling uncertainty.

(a) shows the ground truth for this simulation. Two different labeling uncertainty are simulated in this simulation. In **(b, d, f),** low labeling uncertainty condition (20 nm) are analyzed for the sum image **(b)**, ldrc-SOFI **(d)**, and bSOFI **(f)** respectively. In **(c, e, g),** high labeling uncertainty (80 nm) are analyzed for the sum image **(c)**, ldrc-SOFI **(e)**, and bSOFI **(g)** respectively. Scale bar: 2 um.
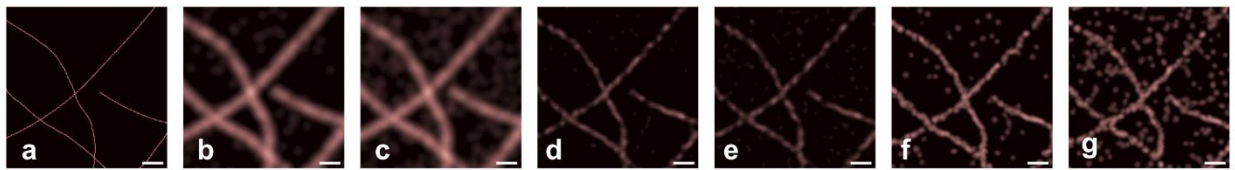
Figure 5.7. Simulation of filaments with different nonspecific binding conditions.

(a) shows the ground truth for this simulation. Nonspecific binded emitters are randomly dropped to the field of view with different density. In **(b, d, f)**, low nonspecific binding density condition are analyzed for the sum image **(b)**, ldrc-SOFI **(d)**, and bSOFI **(f)** respectively. In **(c, e, g)**, high nonspecific binding density condition are anlayzed for the sum image **(c)**, ldrc-SOFI **(e)**, and bSOFI **(g)** respectively. Scale bar: 2 um.
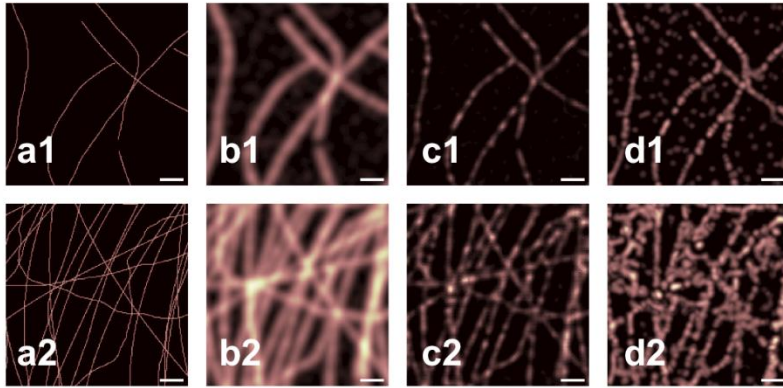
Figure 5.8. Simulation with different filaments density

(**a1, a2**) are the ground truths for different feature of filaments. In (**b1, c1, d1**), low filaments density condition are analyzed for the sum image (**b1**), ldrc-SOFI (**c1**), and bSOFI (**d1**) respectively. In (**b2, c2, d2**), high filaments density conditions are analyzed for the sum image (**b2**), ldrc-SOFI (**c2**), and bSOFI (**d2**) respectively. Scale bar: 2 μm.

Chapter 6. Deconvolution

One extra bonus that high order SOFI provides is an estimation of the point spread function (PSF) of the optical system. In our case the image is always a convolution between the PSF and a ground truth image that is formed by (1) the actual emitters in the case of original image (2) virtual emitters in the case of high order SOFI cumulant and moments as discussed in the previous chapters. With the information of PSF we can try to solve an inverse problem to seek for the corresponding ground truth image, the algorithm to solve such an inverse problem is deconvolution.

If we use g to represent for the ground truth image, and use U to represent for the PSF, we have:

$$g \otimes U = I \tag{6.1}$$

where I is the image to be deconvolved. In our case I is the high order SOFI image, and U is the PSF of the corresponding order. In the case of nth order SOFI cumulant or moment, the PSF U is the nth power of the original PSF. In other words, if we use Gaussian approximation of the PSF, the nth order SOFI image will carry a PSF that has $\sqrt{n}$ fold narrower Gaussian width.

Let U be a Gaussian function, we know that:

$$U^{\frac{1}{a_1}} \otimes U^{\frac{1}{a_2}} \otimes \cdots \otimes U^{\frac{1}{a_n}} \propto U^{\frac{1}{a_1+a_2+\cdots+a_n}} \tag{6.2}$$

Here we design $\{a_i\}$ as described below:

$$\frac{1}{a_n} = \frac{\lambda^n}{\lambda-1} \quad \text{with } \lambda > 1 \tag{6.3}$$

Such that we have:

$$\sum_{i=1}^{\infty} a_i = \sum_{i=1}^{\infty} \frac{\lambda - 1}{\lambda^n} = 1 \qquad (6.4)$$

Substitute equation (6.3) and equation (6.4) into equation (6.2), we get:

$$U^{\frac{\lambda}{\lambda-1}} \otimes U^{\frac{\lambda^2}{\lambda-1}} \otimes \cdots \otimes U^{\frac{\lambda^n}{\lambda-1}} \propto U \qquad (6.5)$$

This means any Gaussian function can be decomposed into a consecutive convolution of a series of narrower Gaussian functions. The concept of our step-wise deconvolution algorithm is to decompose the overall PSF into a series of small PSFs, and deconvolve them one after another, such that for each individual deconvolution step it is a lighter deconvolution task, because the target is more similar to the input image. Here we want to find a design for the power series $\{a_i\}$ such that the summation of the a_i series equals to one.

Chapter 7.   Multi-order Cumulant Analysis of SOFI (MOCA-SOFI)

In this section, we will talk about how to use SOFI cumulant of multiple orders to construct an inverse problem to achieve point spread function estimation, and solve for the spatial distribution of blinking parameters of emitters in the field of view. This version of SOFI utilizes multi-order cumulant analysis and we dub it as MOCA-SOFI.

The nth order SOFI cross-cumulants are cumulants calculated from a group of different pixels from different locations. Intrinsically, the choice of the group of pixels used for $SOFI - XC_n$ computation can either be n distinct pixels, or less than n pixels where part of the pixel is used more than once. $SOFI - XC_n$ encodes information of the PSF, that can be used either for either deconvolution of the image, or other purposes like sample parameter estimation as discussed in the previous section. In this section, we are going to talk about how to get a PSF estimation from $SOFI - XC_n$ values calculated from cross-correlations from a group of pixels. We'll first discuss the theory of SOFI with cross-correlations, based on which we'll migrate to a global fitting approach to estimate the PSF of our optical system.

7.1.   Understanding SOFI cross-cumulants

First, let's write down the fluorescence signal generated by N emitters captured at location $\vec{r}$, denoted as $F(\vec{r})$, as follows:

$$F(\vec{r}) = \sum_{k=1}^{N} U(\vec{r} - \vec{r}_k)\epsilon_k b_k(t) \tag{7.1}$$

Where k is the emitter index, $U(\vec{r})$ is the point spread function of the optical setup, ϵ_k is the on-

time brightness of kth emitter and $b_k(t)$ is the blinking profile of kth emitter. Now if we want to calculate the nth order cross-cumulant (XC_n) using the fluorescence signal captured from n pixel locations (Consider time lags all equal to 0):

$$F(\vec{r}_1), F(\vec{r}_2), ..., F(\vec{r}_n) \tag{7.2}$$

The nth order cumulant is thus denoted as:

$$XC_n(\vec{r}_1, \vec{r}_2, ..., \vec{r}_n) = \sum_{k=1}^{N} U(\vec{r}_1 - \vec{r}_k) U(\vec{r}_2 - \vec{r}_k) \cdots U(\vec{r}_n - \vec{r}_k) \epsilon_k^n \omega_{n,k} \tag{7.3}$$

Now given that $U(\vec{r})$ is the point spread function of the optical system that can be assumed as a Gaussian function:

$$U(\vec{r}) = \exp\left(-\frac{\vec{r}^2}{2\sigma^2}\right) \tag{7.4}$$

We can simplify the expression of $U(\vec{r}_1 - \vec{r}_k) U(\vec{r}_2 - \vec{r}_k) \cdots U(\vec{r}_n - \vec{r}_k)$ in equation (7.3) as follows:

$$U(\vec{r}_1 - \vec{r}_k) U(\vec{r}_2 - \vec{r}_k) \cdots U(\vec{r}_n - \vec{r}_k)$$

$$= \exp\left(-\frac{(\vec{r}_1 - \vec{r}_k)^2}{2\sigma^2} - \frac{(\vec{r}_2 - \vec{r}_k)^2}{2\sigma^2} - \cdots - \frac{(\vec{r}_n - \vec{r}_k)^2}{2\sigma^2}\right) = \exp\left(-\frac{\sum_{i=1}^{n}(\vec{r}_i - \vec{r}_k)^2}{2\sigma^2}\right) \tag{7.5}$$

Now Let's simplify the expression of $\sum_{i=1}^{n}(\vec{r}_i - \vec{r}_k)^2$:

$$\sum_{i=1}^{n}(\vec{r}_i - \vec{r}_k)^2 = \sum_{i=1}^{n}\vec{r}_i^2 + 2\sum_{i=1}^{n}\vec{r}_i\vec{r}_k + n\vec{r}_k^2$$

$$= n\left(\left(\frac{1}{n}\sum_{i=1}^{n}\vec{r}_i\right) - \vec{r}_k\right)^2 + \sum_{i=1}^{n}\vec{r}_i^2 - \frac{1}{n}\left(\sum_{i=1}^{n}\vec{r}_i\right)^2$$

$$= n\left(\vec{r}_{gc} - \vec{r}_k\right)^2 + \frac{1}{n}\sum_{i=1}^{n}\sum_{j=i+1}^{n}\left(\vec{r}_i - \vec{r}_j\right)^2 \tag{7.6}$$

where $\vec{r}_{gc} = \dfrac{1}{n}\sum\limits_{i=1}^{n}\vec{r}_i$

We have $\vec{r}_{gc}$ as the geometry center of the group of pixels selected to compute our nth order SOFI with cross-cumulant $SOFI - XC_n$. Combining equation (7.3) – equation (7.6), we get:

$$XC_n(\vec{r}_1, \vec{r}_2, ..., \vec{r}_n)$$

$$= \exp\left(-\frac{1}{2\sigma^2 n}\sum_{i=1}^{n}\sum_{j=i+1}^{n}(\vec{r}_i - \vec{r}_j)^2\right)\sum_{k=1}^{n}\left(\exp\left(-\frac{(\vec{r}_{gc} - \vec{r}_k)^2}{2\left(\dfrac{\sigma}{\sqrt{(n)}}\right)^2}\right)\epsilon_k^n \omega_{n,k}\right) \tag{7.7}$$

In order to simplify the discussion, we introduce the following notations:

$$f_1 = \exp\left(-\frac{1}{2\sigma^2 n}\sum_{i=1}^{n}\sum_{j=i+1}^{n}(\vec{r}_i - \vec{r}_j)^2\right) \quad \text{and} \quad f_2 = \sum_{k=1}^{n}\left(\exp\left(-\frac{(\vec{r}_{gc} - \vec{r}_k)^2}{2\left(\dfrac{\sigma}{\sqrt{(n)}}\right)^2}\right)\epsilon_k^n \omega_{n,k}\right) \tag{7.8}$$

We can see that the first exponential factor f_1 is defined by the locations of pixels used to compute XC_n, and was previously identified as the distance factor [ref]. The second factor f_2 is equivalence to a virtual fluorescence signal collected at position $\vec{r}_{gc}$ that was generated by virtual

emitter at the same location as in the sample, but instead of having an intensity of ϵ_k, these virtual

emitters now have intensity of $\epsilon_k^n \omega_{n,k}$ for the kth emitter. It is worth noticing here that now the

width of the PSF in this XC_n result shrank by a factor of $\sqrt{(n)}$ compared to that of the original

PSF.

7.2. Estimation of PSF with global fitting approach (Theory)

In this section, we will start with a general discussion of PSF estimation, by combining

$SOFI - AC_n$ of different orders, $SOFI - XC_n$ with different order and different choices of pixel

combinations, to perform a global fitting. An example will be discussed in the next subsection to

demonstrate the proposed approach with SOFI-AC$_2$ and SOFI-XC$_2$.

First, let's write down the mathematical expression of $SOFI - AC_n$ and $SOFI - XC_n$ values:

$$
\begin{aligned}
AC_n(\vec{r}) &= \sum_{k=1}^{N} U^n(\vec{r} - \vec{r}_k)\epsilon_k^n \omega_{k,n} \\
XC_n(\vec{r}_1, \vec{r}_2, ..., \vec{r}_n) &= \exp\left(-\frac{1}{2\sigma^2 n}\sum_{i=1}^{n}\sum_{j=i+1}^{n}(\vec{r}_i - \vec{r}_j)^2\right)\sum_{k=1}^{n}U^n(\vec{r}_{gc} - \vec{r}_k)\epsilon_k^n \omega_{n,k}
\end{aligned}
\tag{7.9}
$$

We can choose the pixel combination $(\vec{r}_1, \vec{r}_2, ..., \vec{r}_n)$ to have geometric center located at $\vec{r}$, in this

case we'll have:

$$
\frac{XC_n(\vec{r}_1, \vec{r}_2, ..., \vec{r}_n)}{AC_n(\vec{r})} = \exp\left(-\frac{1}{2\sigma^2 n}\sum_{i=1}^{n}\sum_{k=i+1}^{n}(\vec{r}_i - \vec{r}_j)^2\right)
$$

where $(\vec{r}_1, \vec{r}_2, ..., \vec{r}_n)$ are selected such that we have:

$$
\frac{1}{n}\sum_{i=1}^{n}\vec{r}_i = \vec{r}
$$

(7.10)

Now simplify our notation with ξ to represent for the distance factor shown below:

$$\xi = \sqrt{\frac{1}{n}\sum_{i=1}^{n}\sum_{j=i+1}^{n}(\vec{r}_i - \vec{r}_j)^2}$$

(7.11)

Where XC_n and AC_n are computed from the fluorescence measurement, ξ can be calculated per group of pixel combinations; the only unknown will thus be σ that characterize the size of PSF. Under this sense, we can perform many different pixel combinations, with multi-order analysis to expand our equation system, a global fitting can thus be applied to yield a robust estimation of PSF.

7.3.   Estimation of PSF with global fitting approach (Simulation verification)

In this demonstration, we use 12 different pixel combinations (Combo A-L), the geometric center $(\vec{r}_{gc})$ of every pixel combination is located at the center pixel. For each pixel combination we can calculate a set of $SOFI - XC_2$ values that is compared to $SOFI - AC_2$ values. The plot of $SOFI - XC_2$ against $SOFI - AC_2$ will thus encode the PSF information as illustrated in table 7.1.

Pixel Combination	$\xi^2 = \frac{1}{2}(\vec{r}_1 - \vec{r}_2)^2$	$\frac{XC_2}{AC_2}$ (slope)
Combo A Combo B	$\xi^2 = 2$	$\exp(-\frac{2}{2\sigma^2})$
Combo C Combo D	$\xi^2 = 4$	$\exp(-\frac{4}{2\sigma^2})$
Combo E Combo F	$\xi^2 = 8$	$\exp(-\frac{8}{2\sigma^2})$
Combo G Combo H Combo I Combo J	$\xi^2 = 10$	$\exp(-\frac{10}{2\sigma^2})$
Combo K Combo L	$\xi^2 = 16$	$\exp(-\frac{16}{2\sigma^2})$

Figure 7.1. PSF estimation using multiple pixel combinations.

Here we demonstrate the strategy to use multiple different pixel combinations to estimate the PSF by comparing the values of $SOFI - XC_2$ and $SOFI - AC_2$. The first column shows 12 different choices of pixel combinations with which $SOFI - XC_2$ will be calculated, and the $SOFI - AC_2$ of the pixel located at the geometry center is calculated as well. In the second column we show the ξ^2 values with ξ defined in equation (7.11). and in the third column we show the theoretical value of the slopes between the $SOFI - XC_2$ and $SOFI - AC_2$ values as a function of σ, which characterize the PSF as defined in equation (7.4). The units of ξ and σ are unit pixel width.

Figure 7.2 shows the plot of $SOFI - XC_2$ with 12 different pixel combinations against the $SOFI - AC_2$ values, the simulation data (**Simulation 7-1**) used in this demonstration is 10 equally spaced quantum dots with power-law blinking statistics emitting at $\lambda = 800nm$, detected with $150\times$ magnification, objective numerical aperture equals to 1.4 and physical size of detectors is $14\mu m$. In this demonstration, the PSF is simulated as a Gaussian function with FWHM defined according to Rayleigh's criteria:

$$FWHM = 0.61\frac{\lambda}{NA} \tag{7.12}$$

Under Gaussian approximation of the PSF, the theoretical width is:

$$\sigma = \frac{FWHM}{2\sqrt{2\cdot\ln 2}} = \frac{0.61\lambda}{NA\cdot 2\sqrt{2\cdot\ln 2}} = 148.02nm$$

The $SOFI - XC_2$ values are calculated for all the 12 different choices of pixel combinations and compared to the value of $SOFI - AC_2$ at the pixel located at their geometry center, the plot is shown in Figure 7.2. The global fitting yields a σ value to be $152.89nm$ while the theoretical input is $148.02nm$.
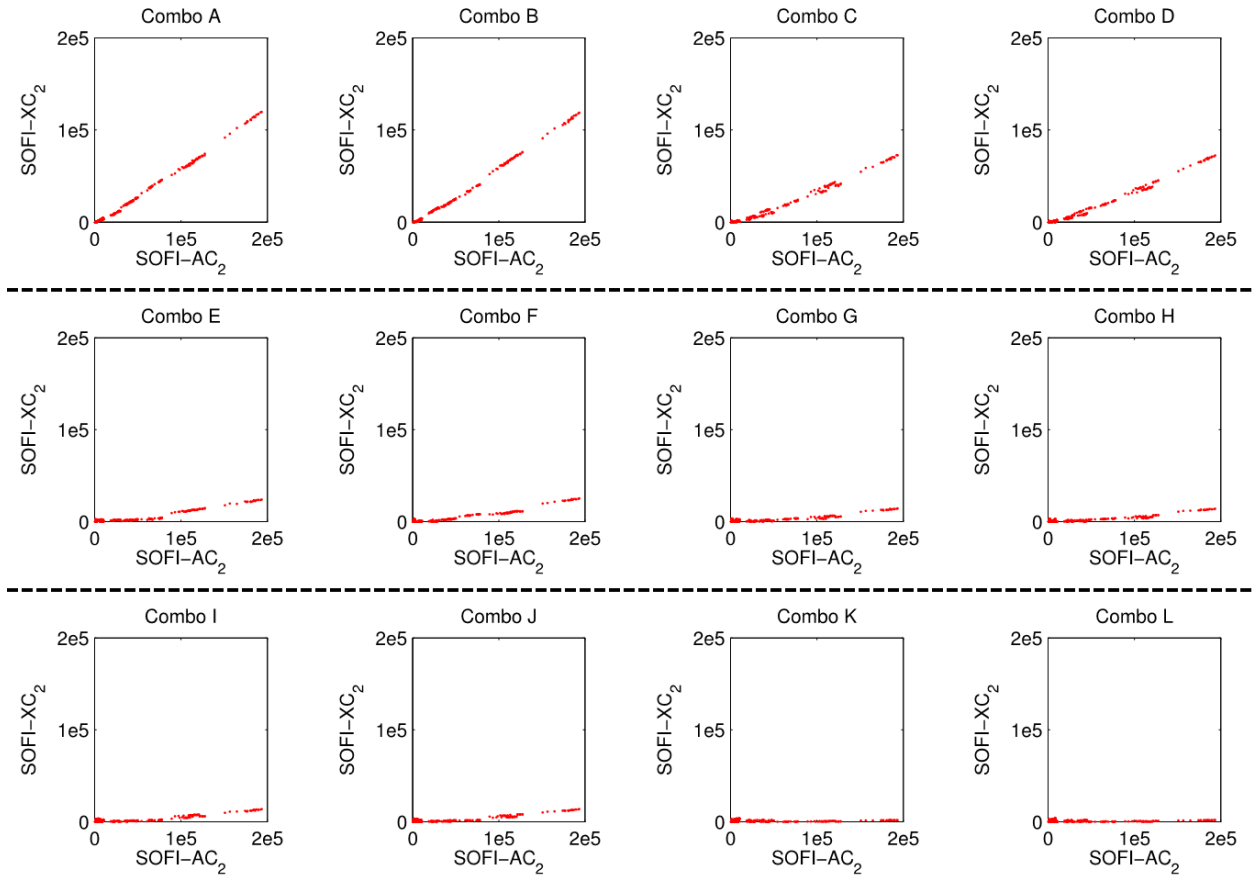
Figure 7.2. Global fitting to achieve PSF estimation.

Here we demonstrate the linear relationship between the between the values of $SOFI - XC_2$ and

$SOFI - AC_2$ values of the pixel combinations discussed in Figure 7.1, the data is calculated from

Simulation 1 (explained in the following context of this chapter). The slopes of all these curves

encodes the information of the PSF size σ as described in the third column of Figure 7.1.

7.4.   Local parameter mapping form multi-order cumulant analysis. (Theory)

In the previous section we discussed how to extract information of PSF, the next step is to use the information of the PSF to estimate blinking statistics of emitters inside the field of view. First, we write down the nth order SOFI image as in the form of summation over N emitters:

$$C_n(\vec{r},\tau_1,\tau_2,...,\tau_{n-1}) = \sum_{k=1}^{N} U^n(\vec{r}-\vec{r}_k)\epsilon_k^n \omega_{n,k}(\tau_1,\tau_2,...,\tau_{n-1}) \qquad (7.13)$$

Where $C_n(\vec{r})$ is n^{th} order cumulant value located at location $\vec{r}$, $U(\vec{r})$ is the point spread function of the imaging system, k is the emitter index, ϵ_k is the brightness of on-state of emitter k and ω_k is the nth order cumulant of the blinking profile of emitter k.

Note here that ϵ_k and $\omega_{k,n}$ are expected to have slow local variation, because emitter brightness and blinking statistics are usually determined by the emitters' local environment. So we can replace the notation of ϵ_k into $\epsilon(\vec{r})$ defined as the on-time brightness of emitters if it is located at $\vec{r}$. Similarly, $\omega_{k,n}$ can be replaced as $\omega_n(\vec{r})$ (defined as the nth order cumulant of the blinking profile of an emitter if it is located at $\vec{r}$. Under this sense, $\epsilon(\vec{r})$ and $\omega_n(\vec{r})$ are functions that encodes information of the local environment that doesn't necessarily follow the spatial distribution of emitters. Introduce another variable $L(\vec{r})$ as follows:

$$L(\vec{r}) = \begin{cases} 1, & \text{when there is an emitter at location } \vec{r} \\ 0, & \text{where there is no emitter at location } \vec{r} \end{cases} \qquad (7.14)$$

So equation (7.13) can be re-arranged into the convolution form is as follows:

$$C_n(\vec{r}, \tau_1, \tau_2, ..., \tau_{n-1}) = \left(\epsilon(\vec{r})^2 \cdot L(\vec{r}) \cdot \omega_n(\vec{r}, \tau_1, \tau_2, ..., \tau_{n-1}) \right) \otimes U^n(\vec{r}) \qquad (7.15)$$

where $\otimes$ indicates the operation of spatial convolution.

Considering the correlation analysis with all the time lags equal to 0, equation (7.15) can be simplified as:

$$C_n = \epsilon^n \omega_n (L \otimes U^n) \qquad (7.16)$$

Where ϵ and ω_n are slow varying variables in space. Here, for each SOFI order number n, we can always calculate the SOFI cumulants C_n from the captured signal, and end-up with one equation as equation (7.16) of three unknowns ($\epsilon(\vec{r})$, $L(\vec{r})$ and $\omega_n(\vec{r})$). If we introduce another notation ρ_{on} to characterize the percentage of time an emitter spent at 'on'-state and dub as 'on'-time ratio, given sufficient statistical significance, different orders of $\omega_n(\vec{r})$ can further be expressed as different functions of $\rho_{on}(\vec{r})$, thus different orders of $C_n(\vec{r})$ is always functions of three identical variables: $\epsilon(\vec{r})$, $L(\vec{r})$ and $\rho_{on}(\vec{r})$. Given the noisy nature of our observation of fluorescence signal measurement, and the intrinsically unlimited number of cumulants that can be computed, we can get an over-determinant equation system. Regression method is thus preferred to solve for our unknown variables rather than a direct mathematical inversion as outlined in [ref bSOFI paper]. In the following discussion, we are going to use a demonstration with cumulants from 2nd order to 7th order. Because SOFI with cross-correlation analysis can give us an estimation of the point spread function U,

and with Gaussian approximation of the point spread function, we have:

$$U^n \otimes U^{\frac{2n}{n-2}} = u^2 \tag{7.17}$$

So we can obtain an equation system as follows:

$$
\begin{aligned}
C_2 &= \epsilon^2 \omega_2 (L \otimes \mathrm{U}^2) \\
C_3 \otimes U^6 &= \epsilon^3 \omega_3 (L \otimes \mathrm{U}^2) \\
C_4 \otimes U^4 &= \epsilon^4 \omega_4 (L \otimes \mathrm{U}^2) \\
C_5 \otimes U^{10/3} &= \epsilon^5 \omega_5 (L \otimes \mathrm{U}^2) \\
C_6 \otimes U^3 &= \epsilon^6 \omega_6 (L \otimes \mathrm{U}^2) \\
C_7 \otimes U^{14/5} &= \epsilon^7 \omega_7 (L \otimes \mathrm{U}^2)
\end{aligned}
\tag{7.18}
$$

Where ω_n follows the expressions below:

$$
\begin{aligned}
\omega_2 &= \rho_{on} - \rho_{on}^2 \\
\omega_3 &= \rho_{on} - 3\rho_{on}^2 + 2\rho_{on}^3 \\
\omega_4 &= \rho_{on} - 7\rho_{on}^2 + 12\rho_{on}^3 - 6\rho_{on}^4 \\
\omega_5 &= \rho_{on} - 15\rho_{on}^2 + 50\rho_{on}^3 - 60\rho_{on}^4 + 24\rho_{on}^5 \\
\omega_6 &= \rho_{on} - 31\rho_{on}^2 + 180\rho_{on}^3 - 390\rho_{on}^4 + 360\rho_{on}^5 - 120\rho_{on}^6 \\
\omega_7 &= \rho_{on} - 63\rho_{on}^2 + 602\rho_{on}^3 - 2100\rho_{on}^4 + 3360\rho_{on}^5 - 2520\rho_{on}^6 + 720\rho_{on}^7
\end{aligned}
\tag{7.19}
$$

Introduce a new notation:

$$X_n = \frac{C_n \otimes U^{\frac{2n}{n-2}}}{C_2} \tag{7.20}$$

Where X_n can be directly computed from fluorescence signal and cross-correlation of fluorescence signal from different pixels. Combining equation (7.20) with equation(7.18) and equation (7.19), we get:

$$X_3 = \epsilon(1 - 2\rho_{on})$$
$$X_4 = \epsilon^2(1 - 6\rho_{on} + 6\rho_{on}^2)$$
$$X_5 = \epsilon^3(1 - 14\rho_{on} + 36\rho_{on}^2 - 24\rho_{on}^3) \qquad (7.21)$$
$$X_6 = \epsilon^4(1 - 30\rho_{on} + 150\rho_{on}^2 - 240\rho_{on}^3 + 120\rho_{on}^4)$$
$$X_7 = \epsilon^5(1 - 62\rho_{on} + 540\rho_{on}^2 - 1560\rho_{on}^3 + 1800\rho_{on}^4 - 720\rho_{on}^5)$$

where all the three associated variables are functions of spatial coordinate $\vec{r}$, but we dropped the $(\vec{r})$ in the expression for simplicity of notations. In the equation system outlined in equation (7.21), $X_n(\vec{r})$ is known, $\epsilon(\vec{r})$ and $\rho_{on}(\vec{r})$ are unknowns, any regression method that solves for polynomial equation system with 2 unknowns can thus be applied to solve for $\epsilon(\vec{r})$ and $\rho_{on}(\vec{r})$. A small window can thus be defined that has the comparable size of U^2 to obtain multi observations, a global fitting method can be applied for more robust fitting of $\epsilon(\vec{r})$ and $\rho_{on}(\vec{r})$. In principal, the resolution of the spatial variation of the unknown variables is limited by the lowest cumulant order utilized to build this equation system. Which means in principal the same approach can be extended with extra higher order cumulants while excluding the lower order cumulant, and instead of performing convolution of the PSF to reach final PSF as U^2, we can redesign the convolution outlined in equation (7.17) and achieve the final PSF size that match to different PSF sizes as shown below:

$$U^n \otimes U^{\frac{mn}{n-m}} = u^m \qquad (7.22)$$

The general goal here is to perform convolution of the higher order cumulants to expand their PSF to match to the size of the lowest order of cumulant used to construct the equation system. Use deconvolution to shrink the lower order cumulants PSF is less preferable because of the lack of reliability in deconvolution performance.

Note here that we are assuming $\epsilon(\vec{r})$, $\rho_{on}(\vec{r})$ are spatially slow varying variables, to be more specific, starting from equation (7.18) we are assuming $\epsilon(\vec{r})$, $\rho_{on}(\vec{r})$ are constant within an area covered by U^2. If the equation system outlined in equation (7.21) is constructed with the lowest cumulant order as m, then we only need to assume $\epsilon(\vec{r})$, $\rho_{on}(\vec{r})$ are constant within an area covered by U^m.

Once we have the information of $\epsilon(\vec{r})$ and $\rho_{on}(\vec{r})$, we can combine it with equation (7.17) and solve for $L \otimes U^n$ that which encode the information of local emitter density.

7.5. Local parameter mapping form multi-order cumulant analysis. (Simulation verification)

In this section, we are going to use the data of Simulation-7.1 to demonstrate the process of the estimation of ρ_{on} and $\epsilon(\vec{r})$ as outlined in the previouse section. The blinking statistics of the Simulation 7-1 is outline din Table 7.1, and the imaging system of the simulation is outlined in the section of "Estimation of PSF with global fitting approach" in this chapter. First, we calculate $SOFI - AC_n$ with the SOFI orders range from 2nd order to 7th order as shown in Figure 7.3. Noting here that in this demonstration, the on-time brightness of all the emitters are identical, the only difference between these emitters are their on-time ratio ρ_{on}. We can see that for different emitters with different blinking statistics, different order cumulants will show difference in $\pm$ signs and amplitudes, as outlined in equation (7.19). We then take the PSF estimation and convolve each order of $SOFI - AC_2$ with $U^{\frac{2n}{n-2}}$, and the images we get is shown in Figure 7.4
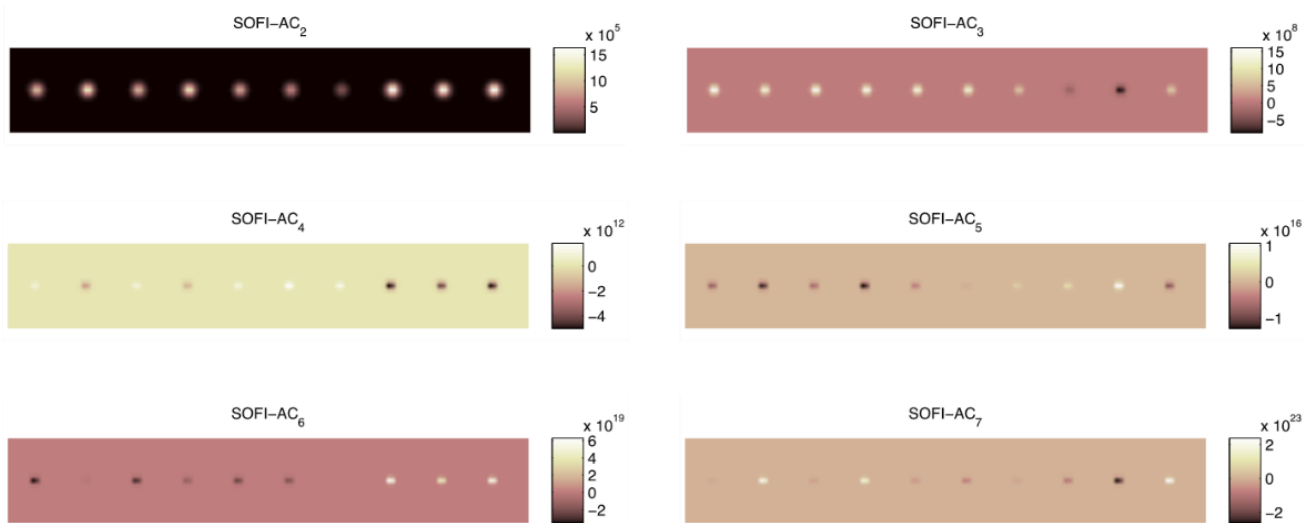
Figure 7.3. SOFI cumulants.

different order cumulant calculated from auto-correlations, $SOFI - AC_n$ with n = 2, 3,...,7. In this

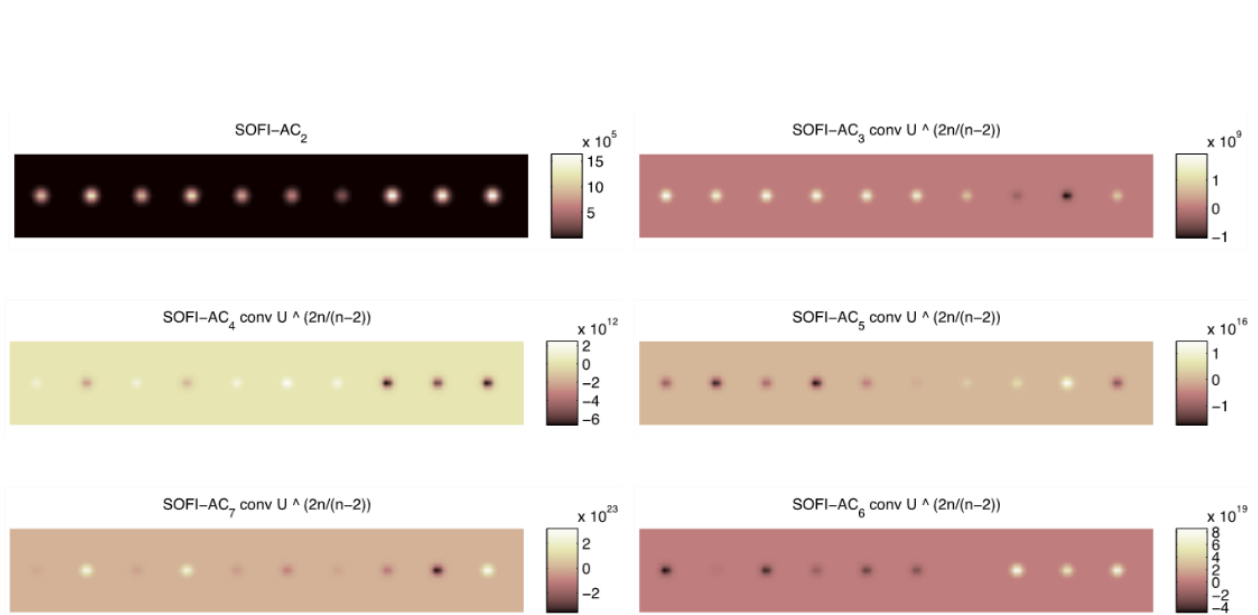simulation. Notice here that the PSF is shrinking with the increase of cumulant order.

Figure 7.4. Images of SOFI-AC$_2$ convolved with $U^{2n/(n-2)}$.

In this figure we show the convolution of different order of SOFI cumulant calculated for simulation 7-1 and shown in Figure 7.3, with different width of Gaussian functions. We can see that in each resulting image the PSF is of the same size.

The next step is to take the output shown in Figure 7,4, and follow the operation outlined in

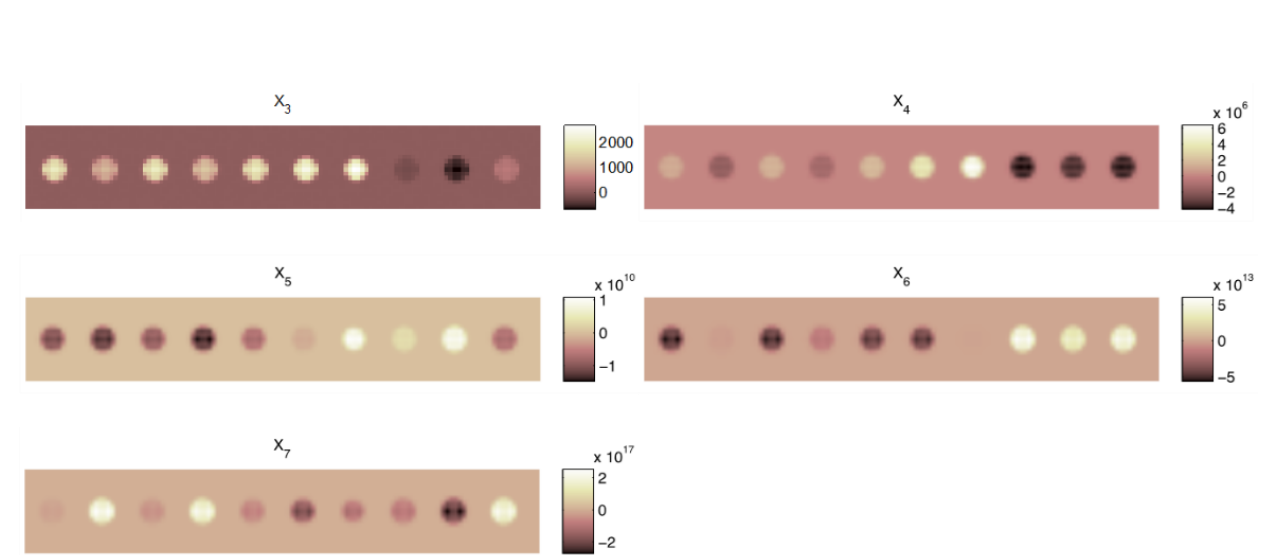equation (7.20) to obtain the five output images ($X_3,..., X_7$) as shown in Figure 7.5:

Figure 7.5. Computed equation system {Xn}.

We can see there the computed $\{X_n\}$ is in the form of images that has pixel intensity encoding

the information of blinking statistics parameters ρ_{on} and ϵ. The information is only encoded in

the area accessible by the emitters in the field of view. So here we only see circular area has the

encoded information while the amplitude of the information in the background region remains

low.

Now we can use these images of $\{X_n\}$ with $n = 3,4,5,6,7$ to solve for the two unknown variables $\epsilon(\vec{r})$ and $\rho_{on}(\vec{r})$ as outlined in equation (7.21). In principal, solving the equation system is an independent problem that any suitable method can be applied. Here we demonstrate the method that is utilized in this demonstration: First, let's reconstruct the equation into the following form:

$$\frac{1}{\epsilon} = \frac{1}{X_3}(1 - 2\rho_{on})$$

$$\frac{1}{\epsilon^2} = \frac{1}{X_4}(1 - 6\rho_{on} + 6\rho_{on}^2)$$

$$\frac{1}{\epsilon^3} = \frac{1}{X_5}(1 - 14\rho_{on} + 36\rho_{on}^2 - 24\rho_{on}^3) \qquad (7.23)$$

$$\frac{1}{\epsilon^4} = \frac{1}{X_6}(1 - 30\rho_{on} + 150\rho_{on}^2 - 240\rho_{on}^3 + 120\rho_{on}^4)$$

$$\frac{1}{\epsilon^5} = \frac{1}{X_7}(1 - 62\rho_{on} + 540\rho_{on}^2 - 1560\rho_{on}^3 + 1800\rho_{on}^4 - 720\rho_{on}^5)$$

We can see that each equation is a curve in a two dimensional space where one axis represents for ρ_{on} and the other axis represents for $\frac{1}{\epsilon}$. This means at each given location $\vec{r}$, the solution of the equation system should be the crossing point of the five curves corresponding to the five equations outlined above. However, since we are dealing with a noisy system here, the five curves do not necessarily cross at the same point in the two dimensional plane. Consequently, an estimation of the solution should be determined. Given that ϵ should be positive, and ρ_{on} should range from 0 to 1, we can draw the curves that follows the form of $f_i(\rho_{on}) = \frac{1}{\epsilon}$ with $i = 3,4,5,6,7$ as follows:

$$f_3(\rho_{on}) = \frac{1}{\epsilon} = \frac{1}{X_3}(1-2\rho_{on})$$

$$f_4(\rho_{on}) = \frac{1}{\epsilon} = \left(\frac{1}{X_4}(1-6\rho_{on}+6\rho_{on}^2)\right)^{\frac{1}{2}}$$

$$f_5(\rho_{on}) = \frac{1}{\epsilon} = \left(\frac{1}{X_5}(1-14\rho_{on}+36\rho_{on}^2-24\rho_{on}^3)\right)^{\frac{1}{3}} \quad (7.24)$$

$$f_6(\rho_{on}) = \frac{1}{\epsilon} = \left(\frac{1}{X_6}(1-30\rho_{on}+150\rho_{on}^2-240\rho_{on}^3+120\rho_{on}^4)\right)^{\frac{1}{4}}$$

$$f_7(\rho_{on}) = \frac{1}{\epsilon} = \left(\frac{1}{X_7}(1-62\rho_{on}+540\rho_{on}^2-1560\rho_{on}^3+1800\rho_{on}^4-720\rho_{on}^5)\right)^{\frac{1}{5}}$$

Now for each given $\vec{r}$, we can have five curves that represents the five equations outlined above in equation (7.24). We can find the optimal ρ_{on} such that $\{f_i(\rho_{on})\,|\,i=3,4,5,6,7\}$ is most closely distributed to be the solution of our equation. In this demonstration, we take the average of the mutual cross points of the five curves. The solution of ρ_{on} and ϵ is find for each pixel across the FOV and is calculated and compared to the values calculated from bSOFI, as demonstrated in Figure 7.6.
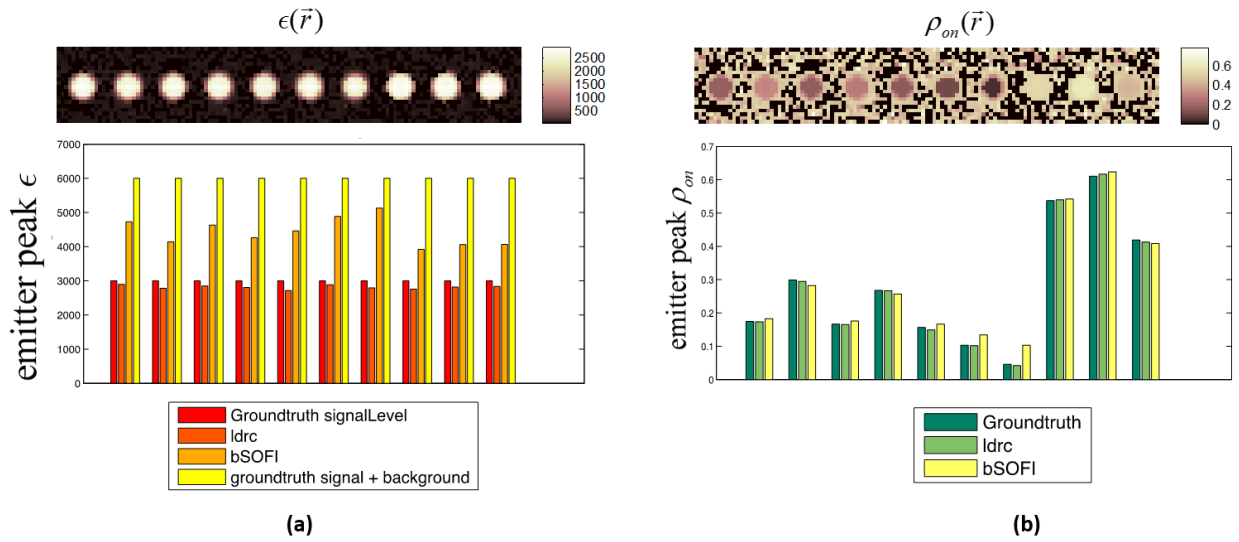
Figure 7.6. Estimation of "on"-state brightness and "on"-time ratio.

The values shown for the 10 emitters in simulation using moca-SOFI, and compared to the performance of bSOFI.

	Brightness	m_{on}	m_{off}	$t_{CutOff}(s)$	$t_{Expo}(s)$	Frame #	Precision(s)
Emitter #1	1	1.45	1.48	10	0.01	1000	0.00025
Emitter #2	1	1.49	1.47	10	0.01	1000	0.00025
Emitter #3	1	1.5	1.49	10	0.01	1000	0.00025
Emitter #4	1	1.43	1.43	10	0.01	1000	0.00025
Emitter #5	1	1.47	1.44	10	0.01	1000	0.00025
Emitter #6	1	1.41	1.41	10	0.01	1000	0.00025
Emitter #7	1	1.48	1.45	10	0.01	1000	0.00025
Emitter #8	1	1.46	1.5	10	0.01	1000	0.00025
Emitter #9	1	1.42	1.46	10	0.01	1000	0.00025
Emitter #10	1	1.44	1.42	10	0.01	1000	0.00025

Table 7.1. Simulation 7.1 blinking statistics.

98

Chapter 8. SOFI 2.0 imaging on fixed cells labeled with quantum dots

In this section, we will discuss the imaging of fixed cells labeled with quantum dots. Either 3T3 cells or Hela cells are cultured in 30mm glass bottom dish until the cell culture reaches about 70% confluency. The cell dish is washed with warm (37C) 1x PBS buffer >4 hours prior to cell fixation and is placed into 37C incubator (5% CO_2) for cells to relax to healthy condition. The cells are then fixed with fixative that contains both formaldehyde and Glutaraldehyde with 1% Triton (detailed recipe for fixative is explained in the protocols section). We labeled alpha-tubulin structure using primary antibody (eBioscience Cat#14-4502-80) that binds to the alpha-tubulin and secondary antibody (ThermalFisher Ref#Q11071MP) that carries quantum dots and binds to the primary antibody. Imaging is performed with either a Nikon setup, or home built TIRF microscope. The SOFI analysis is performed with all the data processing discussed in the previous chapter sand the displayed result we dub as SOFI-2.0 result. As shown in Figure 8.1 we have shown the performance of SOFI 2.0 on QD labeled fixed cells.
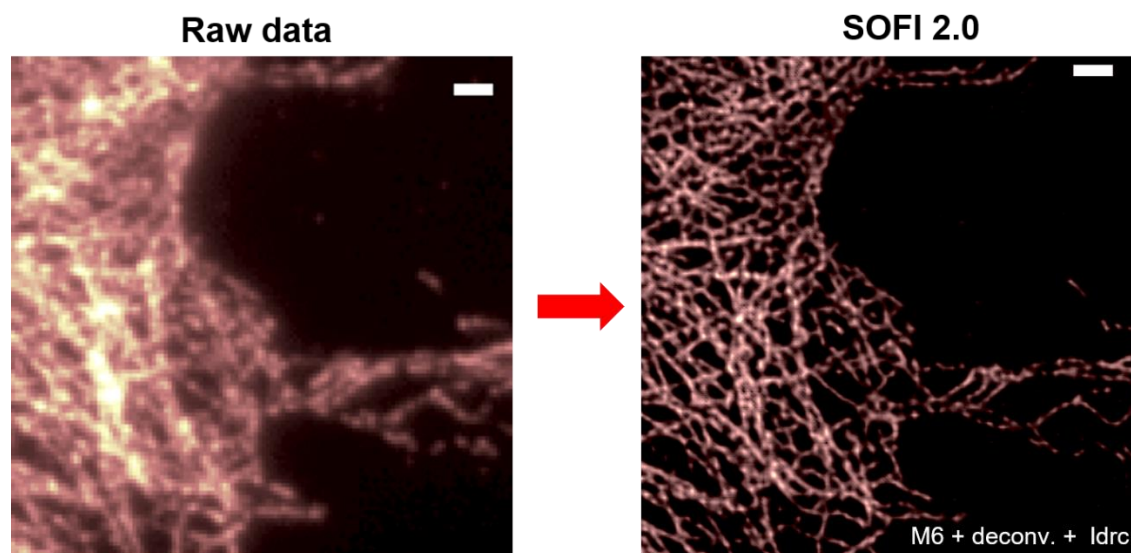
Figure 8.1. Performance of SOFI 2.0 on fixe 3T3 cell. Scale bar: 1.6 μm.

Fixative is made with as described in the below:

Prepare 5M sodium chloride solution, 1M magnesium chloride solution, 200mM MES solution, 2x sucross (22.2% w/v) and 25mM EGTA. In the preparation of the EGTA solution, it is important to adjust the PH of the solution to be 8 such that EGTA can dissolve completely. The dissolving process may take up to 20 minutes with constant stir, and the PH value needs to be adjusted over the process. Mixing the following ingredients to make 100ml 4xCB buffer: 20mL 200mM MES, 11.25mL 5M sodium chloride, 20mL 25mM EGTA, 1mL 1M $MgCl_2$ and 47.25ml de-ionized water filtered with 0.22um filter. Then 50ml Fixative is prepared with 12.5mL 4xCB Buffer, 12.5mL 2x Sucrose, 12.5mL 1% Triton, 1mL 25% Glutaraldehyde, 4.5mL 36.5% Formaldehyde and 7ml deionized water filtered with 0.22um filter.

Fixative solution is store at 4°C and warmed at 37C water bath prior to usage.

Chapter 9. SOFI 2.0 on live cells

We performed SOFI analysis on live cell with all the improvement we have discussed in the previous sections including moments reconstruction, local dynamic range compression and step wise deconvolution (thus we dub this advanced version of SOFI as SOFI2.0). Here we demonstrate the live cell imaging using 3T3 cells with actin labeled through fluorescence protein fusion of DronpaC12 (unpublisehd) with β-Actin. The cells are cultured in 35mm glass bottom dish before transfection of the plasmid containing the sequence of DronpaC12-(GGGGS)x3 linker -β-Actin fusion protein. The cells are transfected when it reaches around 90% confluency with lipofectamin 2000. The cells are incubated for 32 to 38 hours before imaging, and the cells are under warm 1x PBS buffer condition while imaging.

As shown in Figure 9.1 where we have shown the image reconstruction of 300 frames. Because we use an epi lamp instead of laser for excitation, the bleaching rate is largely attenuated which allow us to acquire data set more than 15 minutes long. The entire movie is divided into individual blocks of 300 frames, where each block is processed independently using SOFI2.0. We can see from Figure 9.2 a zoom-in region from the dataset shown in Figure 9.1 at different time instance. During the data acquisition, the exposure time per frame is 50 miliseconds and each block of 300 frames gives one instance of the SOFI2.0 reconstruction, that together can constitute a movie with super resolution as shown in SI movie 1 (Chapter9_SOFImovie.avi).
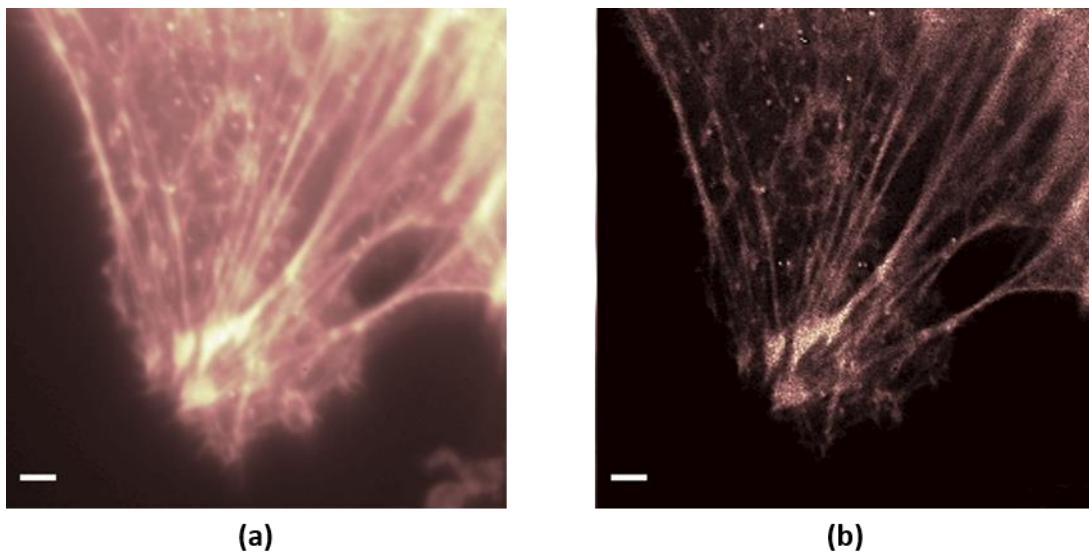
(a)   **(b)**

Figure 9.1. SOFI 2.0 performance on live cell.

Here we present a live cell imaging result of SOFI 2.0 compared to the time average frames. (a)

is the time average of the 300 frames, and (b) is the SOFI 2.0 result processed from the 300

frames. Each frame is 50 ms exposure time and signal accumulation. The shown region is a focal

adhesion site of a 3T3 cell. The labeled feature is β - actin, labeled with DronpaC12 through

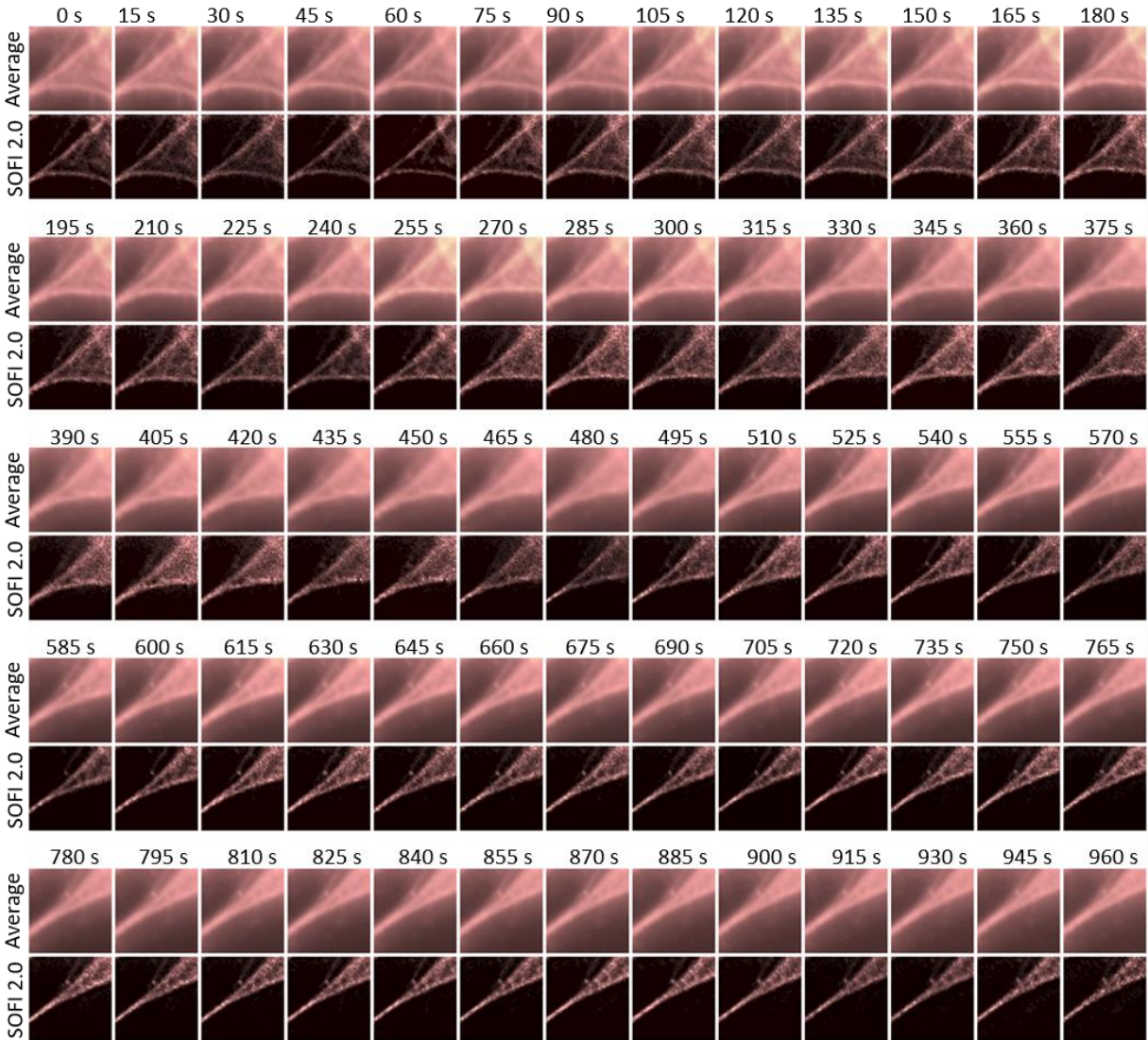protein fusion. Cell is imaged in 1x PBS buffer with 90x magnification. Scale bar 1.92 μm .

Figure 9.2. SOFI 2.0 reconstruction compared to average image at different time instances.

Here we show a zoom-in region of the reconstructed SOFI 2.0 movie of the same sample shown in Figure 9.1. The size of the field of view is $8\mu m \times 8\mu m$. Raw data of a movie with 19200 frames are processed, where the entire movie is divided into 65 individual blocks with 300 frames per block. Each block is processed with SOFI 2.0 individually and yield an output image that represents an instance in the reconstructed SOFI 2.0 movie. We have shown above all 65 instances of SOFI 2.0 results and the corresponding time average result as labeled in the figure.

Chapter 10. Discussion

In this project, several advancement of SOFI is presented that together constitute what we dub as SOFI 2.0. The performance of SOFI 2.0 has been demonstrated on fixed cells as well as live cell imaging, especially the ability of SOFI 2.0 to produce a super resolution movie at a time resolution of 15 seconds per frame, and with continues imaging of more than 15 minutes. We look forward for follow up research to study and unveil new biological discoveries with the ability to visualize dynamic process with super-resolution provided by SOFI 2.0.